Modelling the effect of sea ice in an ocean tide model

Vasulkar, Amey; Verlaan, Martin; Slobbe, Cornelis; Kulikov, Mikhail

Important note
To cite this publication, please use the final published version (if applicable).
Please check the document version above.

Modelling the effect of sea ice in an ocean tide model

Amey Vasulkar [a,c,*], Martin Verlaan [a,c], Cornelis Slobbe [b], Mikhail Kulikov [d]

[a] *Delft Institute of Applied Mathematics, TU Delft, Building 36, Mekelweg 4, Delft, 2628CD, Zuid-Holland, The Netherlands*
[b] *Civil Engineering and Geosciences, TU Delft, Stevinweg 1, Delft, 2628CN, Zuid-Holland, The Netherlands*
[c] *Deltares, Boussinesqweg 1, Delft, 2629HV, Zuid-Holland, The Netherlands*
[d] *Shirshov Institute of Oceanology of Russian Academy of Sciences, Moscow, Russia*

ARTICLE INFO

ABSTRACT

Arctic sea ice leads to a significant dissipation of tidal energy, necessitating its inclusion in global tidal models. However, most global tidal models either neglect or only partially incorporate the impact of sea ice on tides. This study proposes a method to model the dissipative forces exerted by sea ice on tides without directly coupling to a sea ice model, yet utilizing sea ice parameters such as thickness and concentration. Our approach involves (re)-categorizing the sea ice cover into regions dominated either by the velocity difference between sea ice and tides (Vertical Shear (VS)) or by the shear from drifting sea ice on tides (Horizontal Shear (HS)), which primarily govern the energy dissipation between tides and sea ice. The subdivision and resulting areas of these HS and VS regions are based on a nondimensional number referred to as the *Friction number*, which is the ratio of the internal stress of the sea ice field to the ice–water frictional stress, and directly depends on the thickness and concentration of the sea ice. The new parameterization is validated through a performance assessment comparing it to a commonly used approach of assuming all the sea ice to be stationary (landfast). The seasonal modulation of the M_2 tidal component, quantified as the March–September difference, serves as the performance metric, demonstrating that the new parameterization has better agreement with observations from altimeter- and tide gauge-derived seasonal modulation. The results indicate that the physics of ice–tide interaction is better represented with the new parameterization of sea ice-induced dissipation, making it suitable for investigating the effects of declining sea ice thickness on tides.

1. Introduction

Numerous studies have investigated the influence of tides on Arctic sea ice dynamics (e.g., Holloway and Proshutinsky (2007) and Luneva et al. (2015), among others). However, there is limited knowledge regarding the impact of sea ice and its decline (Perovich and Richter-Menge, 2009; Meier, 2016) on future global tides and surges. Most global or regional ocean tide models do not model the effect of sea ice on tides (e.g., Lyard et al., 2021; Padman and Erofeeva, 2004 and Pal et al., 2023), and as such, are not able to study the impact of sea ice and its decline on tides. Recent regional studies by Overeem et al. (2011) and Lintern et al. (2013) have demonstrated that the reduced sea ice extent provides greater fetch and wave action and, as such, allows higher storm surges to reach the shore. Other regional studies (St-Laurent et al., 2008; Kagan and Sofina, 2010; Müller et al., 2014; Kleptsova and Pietrzak, 2018; Kulikov et al., 2020) have shown a seasonal modulation of tides due to friction between the sea ice–tide interface. Bij de Vaate et al. (2021) observed in a global study a significant impact on the seasonal modulation of the M_2 tide by considering only the Arctic landfast ice.

To assess the impact of Arctic sea ice decline on global tides, global hydrodynamic tidal models should model the effect of sea ice on tides. Sea ice is known to cause a frictional dissipation force on tides, resulting in a loss of tidal energy (St-Laurent et al., 2008). Such loss, coupled with the seasonal and inter-annual variations in sea ice extent, leads to a modulation of tides. In the past, tidal models did not consider such modulation of tides from sea ice, assuming that the model errors were much larger than any modulation (Kleptsova and Pietrzak, 2018). As such, these models either ignored sea ice or assumed a constant yearly mean sea ice cover. In the latter case, the models incorporate the effect of dissipation from sea ice as an additional term, similar to sea bed (bottom) frictional stress.

A rigorous approach to include the effect of sea ice exploits a global 3D coupled ocean tide–sea ice model, resolving the effects of sea ice on tides and vice versa (e.g., STORMTIDE Müller et al. (2014), FESOM2.1 Song et al. (2023)). However, these models employ coarse grids, leading to less accurate tidal dynamics (Song et al., 2023), while increasing grid resolution significantly increases computational

---

costs. Despite the 3D nature of these ice–ocean models, they do not necessarily exhibit greater accuracy compared to most high-resolution 2D global tidal models. These 2D global tidal models have also improved in the past couple of decades, owing to improved modelling and data assimilation from satellite altimetry (Stammer et al., 2014). Nevertheless, an accurate representation of tides remains a challenge for these models in the poleward regions (above 66° latitude) (Stammer et al., 2014; Kleptsova and Pietrzak, 2018).

In the current state-of-the-art 2D hydrodynamic tidal models, the effect of sea ice dissipation and its resulting modulation is included by using a monthly mean sea ice cover instead of a yearly mean (time invariant) version, with sea ice assumed to be fixed, i.e., landfast ice (e.g., Cancet et al. (2018), Kleptsova and Pietrzak (2018)). The ice-friction stress is then simulated in Kleptsova and Pietrzak (2018) using approaches proposed by Dupont et al. (2002), Dunphy et al. (2008) and Collins et al. (2011), combining it with bottom frictional stress and varying the cumulative drag coefficient based on sea ice concentration. In contrast, Cancet et al. (2018) simply multiplied the bottom frictional stress by a factor of 2 in the region covered by sea ice. While these studies considered the entire sea ice cover/field for the month, Bij de Vaate et al. (2021) only considered monthly landfast sea ice cover. There, the ice–water frictional stress was again modelled by adding extra friction to the bottom frictional stress in the region of the landfast sea ice cover.

However, there are two main issues with these approaches. Firstly, the sea ice field is not entirely fixed, but partly fixed and partly drifting. In fact, only about 12% of the Northern Hemisphere sea ice is fixed/landfast (Mahoney, 2018). Modelling the ice–water frictional stress from drifting sea ice in a 2D tidal model requires a relative velocity between sea ice and water as input (Pease et al., 1983). For such drifting sea ice, the fixed sea ice cover assumption is physically incorrect and would lead to larger dissipation and erroneous results. The second issue is that these parameterizations do not include sea ice parameters like thickness and concentration, and as such, are not equipped to deal with the effect of the spatio-temporal variability of these parameters. In fact, the sea ice is thinning at a rapid rate with large variability (Mallett et al., 2021) in the Arctic. It should be noted here that Kleptsova and Pietrzak (2018) do include the sea ice concentration parameter in an indirect way through the drag coefficient.

The main objective of this paper is to present and analyse a new physically consistent sea ice parameterization that models the effect of sea ice-induced dissipation, incorporating sea ice thickness and concentration. Unlike the traditional division of the sea ice field into landfast and drifting categories with their corresponding dissipation effects, this parameterization identifies two distinct dissipation regimes. The first is referred to as Vertical Shear (VS), representing the dissipation arising from the velocity difference between sea ice and tides, where sea ice is either fixed (landfast) or drifting so slowly that it can be considered almost fixed (referred to as near-stationary sea ice). The second regime, known as Horizontal Shear (HS), accounts for dissipation due to the shear from drifting sea ice. The latter is modelled by integrating the ice–water momentum equations, similar to Heil and Hibler (2002), resulting in a dissipative sea ice viscous internal stress term. The new parameterization addresses the two issues previously mentioned, i.e. the sea ice field as fixed and no consideration of the sea ice parameters. This is achieved by considering horizontal shear dissipation from drifting sea ice, separate from the vertical shear associated with fixed or near-stationary sea ice. Furthermore, the modelling of the horizontal shear also requires the sea ice thickness and concentration fields.

The new parameterization is implemented in the Global Tide and Storm Surge Model (GTSM, Verlaan et al. (2015), Muis et al. (2016)), and its performance is assessed by comparing the model-derived seasonal modulation of the M_2 tide with altimeter- and tide gauge-derived

modulations for the years 2012, 2017, and 2019. These years were chosen because they represent the maximum, minimum, and average differences in ice extent between March and September. Note that the seasonal modulation of the M_2 tide is quantified as the March–September differences in tidal amplitudes and phases.

Moreover, a sea ice field is traditionally subdivided into Landfast sea ice and Drifting sea ice regions. The drifting sea ice field is further subdivided into free drift sea ice and sea ice drifting under strong internal stresses. Such a division is also observed in Vasulkar et al. (2022), where it is noted that the dissipation from free drift sea ice on tides is (almost) negligible under low wind conditions. Meanwhile, in the absence of winds, the sea ice exerts no dissipation on tides (McPhee, 1978; Leppäranta, 2011b; Vasulkar et al., 2022). This implies that only landfast sea ice and sea ice drifting under strong internal stresses cause dissipation on tides. Following McPhee (1980), Leppäranta and Omstedt (1990), one can approximate, in a quantitative sense, that the sea ice field with concentrations less than 0.8 can be assumed to be free drift sea ice. Hence, in this paper, sea ice fields with concentrations above 0.8 will be considered, which would then be either landfast sea ice or sea ice drifting under strong internal stresses.

The paper is organized as follows: Section 2 describes the dataset and model (GTSM) used in this study. Section 3 provides the detailed theory of our approach to model the dissipation of sea ice. Section 4 presents the results and discussions of the validation. Section 5 summarizes and concludes the main findings of this research.

2. Data and models

2.1. Sea ice dataset

A global ocean reanalysis product from the Copernicus Marine Service (Copernicus Marine Service, 2019), having the GLORYS model underneath is used for the parameterization in this study. This product provides monthly mean sea ice thickness and concentration values in a gridded format and, is based on a global numerical model that includes the assimilation of sea ice concentration, among others. The years 2012, 2017, and 2019 were selected because most sea ice datasets have shown sufficient resolution and accuracy in the past decade, i.e.,2010–2020. Additionally, the March–September differences in monthly sea ice extent (obtained from NSIDC (Fetterer et al., 2017)) were maximum for 2012 (≈ 11.6 million km^2) and minimum for 2017 (≈ 9.4 million km^2), while the difference for 2019 is (almost) the average of the two extremes (≈ 10.3 million km^2). The sea ice field with concentration larger than 0.8 is plotted for the year 2019 (Fig. 1).

Although the GLORYS model includes the assimilation of sea ice concentration, it is known to suffer from inaccuracies. In particular, sea ice thicknesses are overestimated in the GLORYS model (Uotila et al., 2019). Ideally, remote sensing-based observational products of sea ice concentration and thickness are more accurate than those derived from the GLORYS model. However, utilizing these datasets presents multiple challenges. Firstly, for our analysis, these products must provide monthly average ice concentrations and thicknesses specifically for March and September in the years 2012, 2017, and 2019. Secondly, integrating different products may lead to inconsistencies; for example, regions with sea ice concentrations greater than 0.8 might lack corresponding thickness data due to disparities in the sources of the products. While interpolation is possible to estimate these thicknesses, it inherently introduces additional errors. Furthermore, the resolution discrepancy between the two products necessitates further interpolation, potentially degrading data quality. In contrast, model-derived products, despite their inherent inaccuracies, offer consistently aligned concentrations and thicknesses with monthly averages. These products also provide the flexibility to generate daily or weekly averages, which might be essential for future enhancements in tidal model simulations. We compare the sea ice extent from the GLORYS model with another dataset in Appendix A and compare the sea ice concentration and thickness from multiple remote sensing products in Appendix B.
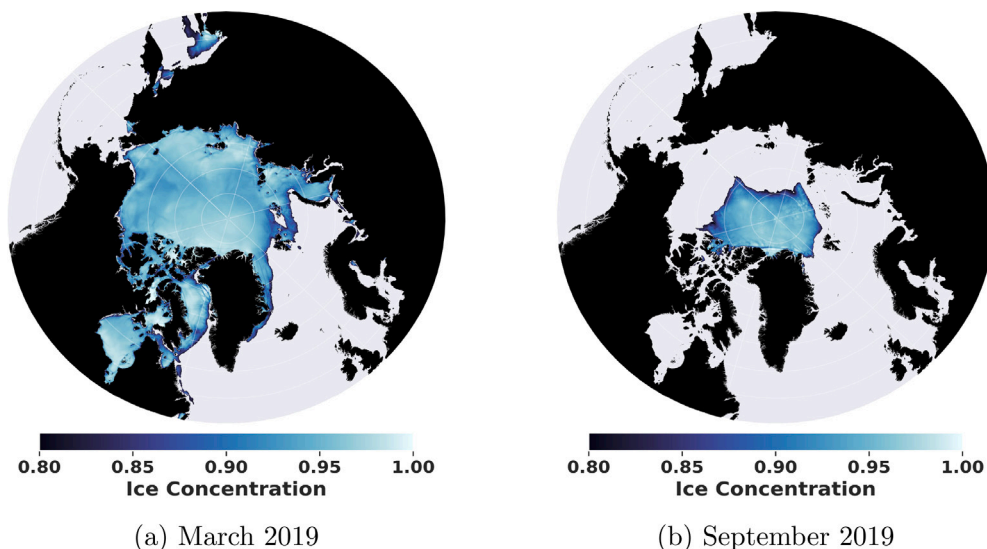
Fig. 1. Sea ice concentration field with values larger than 0.8 for March and September 2019 obtained from a global ocean reanalysis product (Copernicus Marine Service, 2019). The sub-figures (Figs. 1(a) and 1(b)) show the March and September distribution.

2.2. Altimeter-derived seasonal modulation in the Arctic

Bij de Vaate et al. (2021) estimated March–September differences in M_2 amplitude and phase from CryoSat −2 and Sentinel-3 altimeter data acquired between June 2010 to August 2019 (CryoSat −2) and between December 2016 to December 2019 (Sentinel-3). The area covered by the altimetry product includes the region north of 60°N and is extended to include the Hudson Bay area; 50°N–60°N, 100°W–45°W (Fig. 7). UTide (Codiga, 2011) was used to perform tidal analysis using the major tides; K_1, O_1, Q_1, P_1, N_2, M_2 and S_2. This altimetry product is observed to exhibit significant spatial variability of seasonal modulation owing to spatial and temporal data scarcity (Bij de Vaate et al., 2021).

The March–September differences capture the *total* seasonal modulation from not only the seasonal sea ice cover but also other external seasonal forcings, i.e., wind forcing, spatial density differences, stratification, and inter-annual variations of sea ice (Bij de Vaate et al., 2021). However, in the Arctic region, many studies have noted that the seasonal sea ice cover is a major contributor to seasonal modulation (Bij de Vaate et al., 2021; St-Laurent et al., 2008; Müller et al., 2014; Kleptsova and Pietrzak, 2018).

2.3. Tide gauge-derived seasonal modulation

This study uses two tide gauge datasets. The first dataset comprises tidal water level predictions at 15-min intervals at 11 locations for the year 2019. These predictions, obtained from the Canadian Hydrographic Service (Fisheries and Ocean Canada-MEDS, 2019) and referred to as *CHS* in this paper, include predictions for 154 locations. We selected these 11 locations because a Fourier Transform of the year-long time series revealed amplitudes larger than 1 cm for the α_2 (H_1) and β_2 (H_2) tidal frequencies, which are satellite constituents responsible for the seasonal modulation of the M_2 tide (Ray, 2022). From these tidal water level predictions at 11 tide gauge locations, we computed M_2, H_1, and H_2 constituents by performing a tidal analysis without considering the nodal factors. The second dataset includes the M_2, H_1, and H_2 tidal amplitudes and phases for 7 tide gauge records provided by Kulikov et al. (2020). The locations and names of the tide gauges for both datasets are shown in Fig. 2.

Using the amplitudes and phases for the M_2, H_1, and H_2 components from both datasets, a year-long series is reconstructed without considering the nodal factors to eliminate interference with the seasonal

modulation. From this reconstructed signal, the monthly average amplitudes and phases for the M_2 component are computed for both March and September (Fig. 9). This tide gauge-derived dataset is referred to as *TG-derived* in this paper.

2.4. Global Tide and Surge Model

The Global Tide and Surge Model version 4.0 (GTSM) (Verlaan et al., 2015; Muis et al., 2016; Irazoqui Apecechea et al., 2017) is utilized to model the effect of sea ice on tides. Developed within the Delft3D Flexible Mesh suite by Deltares, the model operates on an unstructured grid that begins with a node at the North Pole and transitions from a resolution of 25 km in the open ocean to 2.5 km near the coasts. This grid configuration prevents singularity at the North Pole caused by a regular longitude–latitude grid. The grid in high latitudes is also thinned in the longitudinal direction to avoid numerical issues. Furthermore, such unstructured grid makes it possible to have high resolution in coastal areas and lower in deeper ocean to achieve acceptable computational costs as noted in Kernkamp et al. (2011).

GTSM employs the depth-averaged shallow water equations with no lateral boundaries like in regional tidal models. The tides are forced by the full tide-generating potential and the model also includes Self Attraction and Loading (SAL) and internal tidal wave drag in parameterized forms as these are important in the larger open oceans (Irazoqui Apecechea et al., 2017). The resulting governing equations for continuity and momentum are:

$$\frac{\partial \zeta}{\partial t} + \nabla \cdot (H_d \boldsymbol{u}) = 0, \tag{1}$$

$$\frac{\partial \boldsymbol{u}}{\partial t} + f\, e^{i\pi/2} \boldsymbol{u} + \boldsymbol{u}.\nabla \boldsymbol{u} = -g\nabla(\zeta_n) + \nu_w(\nabla^2 \boldsymbol{u}) + \frac{\boldsymbol{\tau_b}}{\rho_w H_d} + \frac{\boldsymbol{\tau_{IT}}}{\rho_w H_d} + \frac{\boldsymbol{\tau_s}}{\rho_w H_d}, \tag{2}$$

where $\zeta(t)$ is the water level relative to the model's reference surface, $\boldsymbol{u}$ is the tidal water velocity, H_d is the total water depth given by $H_b + \zeta$ with H_b being the bathymetry, $\nu_w(25\,\mathrm{m^2 s^{-1}})$ is the horizontal kinematic viscosity of water, ρ_w is the density of water, f is the Coriolis parameter, g is the acceleration due to gravity, and $\zeta_n = \zeta - \zeta_{eq} - \zeta_{sal}$, where ζ_{eq} is the equilibrium tide, ζ_{sal} is the SAL effect, $\boldsymbol{\tau_b}$ is the bottom frictional stress, $\boldsymbol{\tau_{IT}}$ is the internal tides frictional stress and $\boldsymbol{\tau_s}$ is the wind stress from atmospheric forcing. In this study, we do not consider surges so the $\boldsymbol{\tau_s}$ forcing is set to zero.

GTSM version 4.0 utilizes the GEBCO2019 gridded bathymetry which includes IBCAOv3 for the Arctic Bathymetry (GEBCO Bathymetric Compilation Group, 2019). The model has been globally calibrated
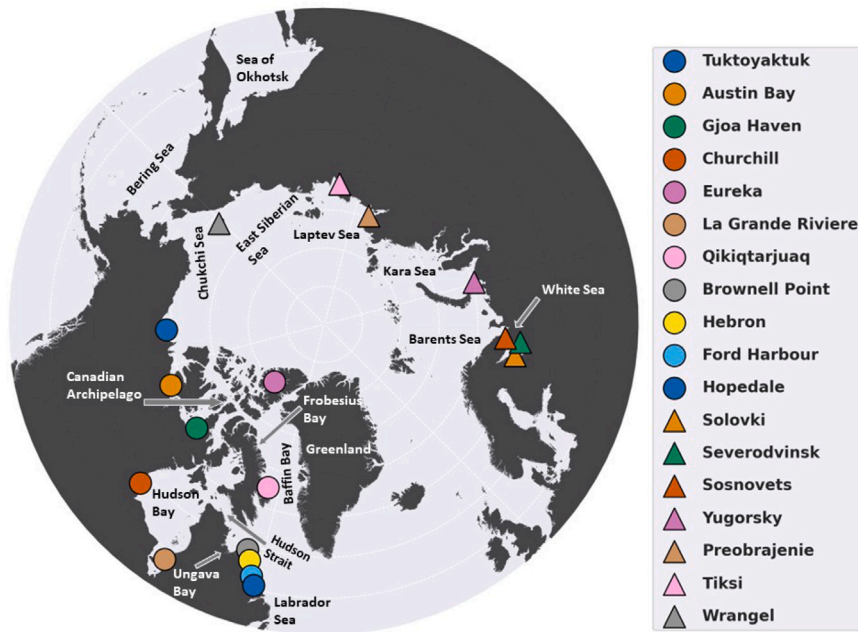
Fig. 2. Tide gauge locations with their respective names in the legend. The dots represent tide gauges from Fisheries and Ocean Canada-MEDS (2019) and triangles represent tide gauges from Kulikov et al. (2020). The names of the regions referred to in the paper are also shown in the figure.

for bathymetry (Wang et al., 2021), using water levels derived from FES2014 (Lyard et al., 2021). This calibrated version 4.0 represents the latest model iteration, offering improved tidal estimates globally, although it is known to exhibit poor accuracy in the Arctic, partly due to the lack of sea ice modelling (Wang et al., 2021).

3. Sea ice parameterization for 2D ocean tide models

3.1. Governing equations with sea ice dissipation

Drifting and landfast sea ice exert different dissipation on tides, and as such, can be modelled separately based on their characteristics. The sea ice-induced dissipation of tides can be incorporated into the momentum equation of the depth-averaged shallow water equations of tidal models. These equations are similar to Eq. (2) in most hydrodynamic 2D models. The resulting momentum equation is given by:

$$\frac{\partial \boldsymbol{u}}{\partial t} + f e^{i\pi/2}\boldsymbol{u} + \boldsymbol{u}.\nabla\boldsymbol{u} = -g\nabla(\zeta_n) + \nu_w(\nabla^2\boldsymbol{u}) + \frac{\tau_b}{\rho_w H_d} + \frac{\tau_{IT}}{\rho_w H_d}$$
$$+ \left[\lambda\frac{\tau_{wi}}{\rho_w H_d} + (1-\lambda)\frac{\nabla.\sigma}{\rho_w H_d}\right], \tag{3}$$

where the terms have same meaning as in Eq. (2) apart from the sea ice terms with $\nabla.\sigma$ being the stress from the horizontal (2D) sea ice internal friction (σ) with dimension force/length and τ_{wi} is the water–ice surface frictional stress from the landfast (fixed) sea ice and is similar to the bottom frictional stress. λ is a parameter that controls the switch between the two shear forcing from sea ice on tides and is responsible for the classification of sea ice into landfast and drifting sea ice.

In the absence of winds, oceanic forcing is the primary cause of sea ice drift. It follows from the equation that landfast sea ice will have a vertical shear owing to the velocity difference in frictional stress, whereas drifting sea ice will have a horizontal shear on tides as a result of its viscous internal stress. At times, the internal stress for compact sea ice is strong enough for the ice to move slowly and be considered (near) stationary. In such scenarios, sea ice exhibits dissipation characteristics similar to those of landfast sea ice, suggesting that a portion of drifting sea ice also shares similar dissipation characteristics as landfast ice.

Therefore, instead of adhering to the traditional classification (Fig. 3), this paper proposes dividing sea ice with a concentration greater than 0.8 into Horizontal Shear (HS) and Vertical Shear (VS) regions. These names reflect the dominant physical interaction between sea ice and tides. The sea ice field must then be classified into these regions and modelled separately in ocean tide models according to the Eq. (3).

3.2. Modelling of sea ice dissipation with classification

It can be shown with a scaling argument on Eq. (3) that the horizontal shear is lower than the vertical shear, with its maximum potentially equalling the vertical shear. Thus, the upper limit of the horizontal shear is vertical shear and this limit serves to divide the sea ice cover into HS/VS regions.

To classify the ice field into the two shear regions, we introduce a non-dimensional number referred to as the *Friction number* (F). It is defined as the ratio of the frictional stress from the sea ice field internal friction and water–ice frictional shear stress with sea ice drift set to zero, i.e.,

$$F = \frac{\nabla.\sigma}{\tau_{wi}}, \tag{4}$$

where the terms are as described above in Eq. (3). The value of F acts as the classification metric and for $F \geq 1$ the upper limit of horizontal shear is reached and the sea ice is almost stationary. Consequently, such sea ice only causes vertical shear on tides and is classified as VS region. Conversely, for $F < 1$ the sea ice is classified as HS region with the dissipation driven by the sea ice internal viscous stress.

Employing F, the switching parameter λ is utilized to classify into HS and VS regions and is defined as:

$$\lambda = H(F - 1), \tag{5}$$

where $H(.)$ is a Heaviside function which gives a binary switching between HS and VS regions based on the value of F.

To calculate F one needs expressions for the two stress terms. The water–ice frictional stress with sea ice velocity set to zero can be modelled similar to the bottom frictional stress. For GTSM, this is given by:

$$\tau_{wi} = \rho_w C_f |\boldsymbol{u}|\boldsymbol{u}, \tag{6}$$
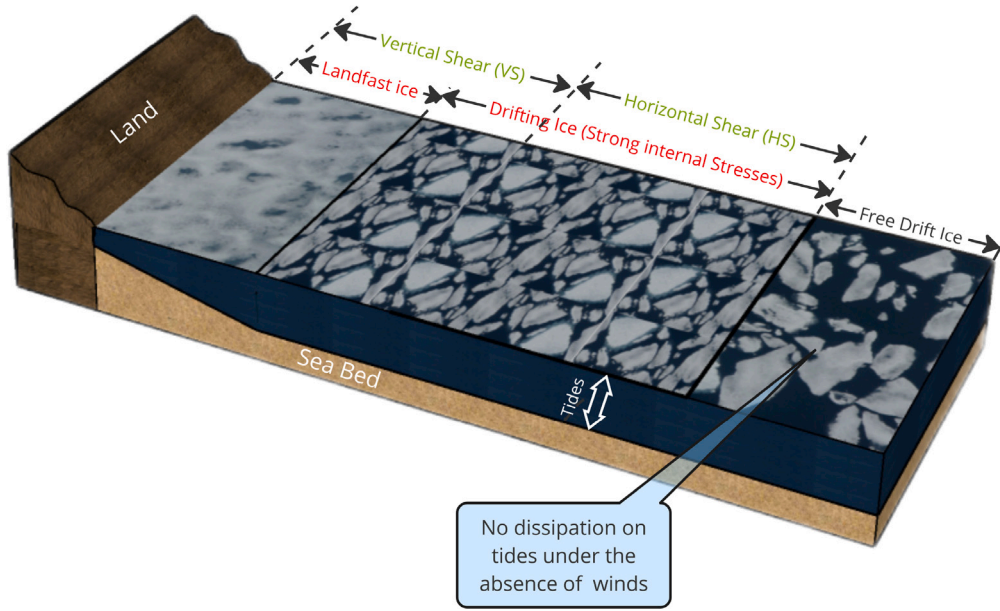
Fig. 3. Pictorial representation of the traditional sea ice field sub-division and the new sub-division into Horizontal and Vertical Shear (HS/VS). This is a representative figure and in reality the ratio of HS/VS can change based on the sea ice parameters and VS can even be larger than the landfast sea ice region.

where C_f is the water–ice drag coefficient.

To model the stress from sea ice internal friction, a sea ice rheology is required. Almost all continuum and geophysical-scale sea ice models employ the Elastic-Viscous-Plastic (EVP) rheology, as proposed by Hunke and Dukowicz (1997) and further discussed in Ólason et al. (2022). This rheology represents a numerically efficient implementation of the Viscous-Plastic (VP) rheology initially proposed by Hibler (1979). However, the EVP rheology is not without its shortcomings. Firstly, its underlying assumptions have been questioned (Coon et al., 2007). Secondly, models employing this rheology have exhibited a larger spread in thickness, concentration, and sea ice drift than what is observed in reality (Chevallier et al., 2017). These limitations have spurred the development of new rheologies, such as the recent Brittle Bingham–Maxwell (BBM) rheology (Ólason et al., 2022), which addresses some of the limitations inherent to the VP rheology. Additionally, there have been several enhancements to the original formulation of the VP rheology itself, aiming to mitigate some of its limitations (e.g., Lemieux et al. (2010), Kimmritz et al. (2016)).

Nonetheless, modelling these rheologies requires significant time and effort, and we believe a simplified version of the VP rheology is more appropriate for our relatively simple parameterization. We adopt the original VP rheology formulation by Hibler (1979), with sea ice modelled as a Newtonian fluid similar to water, i.e., sea ice is assumed to be linear, viscous, and incompressible. Such a Newtonian approximation, initially proposed by Laikhtman (1958), is not representative of sea ice behaviour but does provide first-order approximations for basin-wide sea ice circulation, as noted in Leppäranta (2011c). Moreover, it simplifies the modelling of sea ice internal stress in tidal models because most tidal models already include modelling for the diffusive viscous stress term of water (a Newtonian fluid), allowing the addition of sea ice horizontal shear viscosity to that term.

Given this Newtonian approximation is a simplified one, the viscous-plastic nature of sea ice is partially represented through the sea ice shear viscosity obtained from Hibler (1979)'s rheology:

$$\sigma = \zeta \epsilon_I + 2\eta \dot{\epsilon} - \frac{P}{2}, \tag{7}$$

where $\zeta(h_i, A) = \frac{P(h_i, A)}{2\Delta_o}$ and $\eta(h_i, A) = \frac{\zeta(h_i, A)}{2e_c^2}$ are the horizontal (2D) bulk and shear viscosities (units kg/s), respectively, P is the strength of the sea ice field, Δ_o is the maximum viscous creep variant, e_c is

the aspect ratio of the yield ellipse of the rheology, h_i is the sea ice thickness and A is the sea ice concentration. The expression for sea ice strength ($P = P^* h_i e^{-C(1-A)}$) leads to an expression for the shear viscosity of sea ice given by:

$$\eta = \frac{P^* h_i e^{-C(1-A)}}{4\Delta_o e_c^2}, \tag{8}$$

where P^* is the compressive strength of compact ice of unit thickness, C is a strength reduction constant for lead opening. This formulation implies that the sea ice internal stress and its resulting dissipation are functions of the spatially and temporally varying sea ice thickness (h_i) and concentration (A).

Using Eq. (8) and assuming that the sea ice internal stress is modelled similarly to the diffusive water internal stress, the friction number F can be written as:

$$F = \frac{\eta(\boldsymbol{\nabla}^2 \boldsymbol{u})}{\rho_w C_f \boldsymbol{u}^2}. \tag{9}$$

Note that the horizontal shear viscosity (η) in the depth-averaged shallow water equations is divided by $\rho_w H$ and hence is dimensionally equivalent to the horizontal kinematic viscosity of water (ν_w)

Further simplification of Eq. (9) is achieved through scaling analysis. Assuming a scaling of $u = Uu^*$, $x = Lx^*$ and $y = Ly^*$ where L is the horizontal length scale, the friction number scales as:

$$F \sim \frac{\eta(h_i, A)U}{\rho_w C_f U^2 L^2},$$

$$F \sim \frac{P^* h_i e^{-C(1-A)}}{4\Delta_o e_c^2 \rho_w C_f U L^2},$$

$$F \sim \alpha_i h_i e^{-C(1-A)}, \tag{10}$$

where α_i is a scaling constant given by the expression:

$$\alpha_i = \frac{P^*}{4\Delta_o e_c^2 \rho_w C_f U L^2}. \tag{11}$$

This expression for F (Eq. (10)) represents an exponential function of sea ice concentration A, linear in sea ice thickness h_i and scales with a constant α_i. Given the concentration and thickness vary spatially and temporally, F is also a function of space and time.

Classification based on F depends on the value of the scaling constant α_i given by Eq. (11). The uncertainties associated with the value
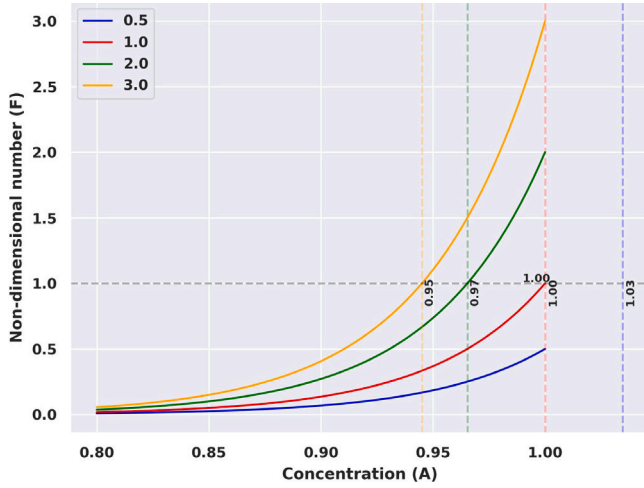
Fig. 4. Plots of non-dimensional friction number (F) versus concentration (A) for $\alpha_i = 1$. The colours correspond to the various sea ice thickness given in the legend. The minimum concentration considered is 0.8. The horizontal grey dotted line is the classification line between HS and VS regions. The abscissa of the point of intersection for each curve with this line gives the corresponding concentration for that thickness which is written along the dotted vertical lines for the respective thicknesses.

of the scaling parameter stem from the uncertainties of the underlying parameters. For instance, P^*, ranges from 10 kPa to 27.5 kPa (Massonnet et al., 2014) showing a large variability. Likewise, the other parameters also have their inherent uncertainties and their values are subject to calibration (See e.g. Massonnet et al. (2014)). Consequently, we instead analyse the range of possible values of the scaling parameter (α_i) based on the resulting classification of sea ice.

Assuming $\alpha_i = 1$, the plot for F versus concentration A (Fig. 4) illustrates exponential curves for fours different sea ice thicknesses, ranging from 0.5 m to 3.0 m.

The horizontal grey dotted line at $F = 1$ demarcates the HS and VS regions with area/region below the line classified as HS and area/region above the line classified as VS region. As per Eq. (10), it is clear that for a sea ice thickness ($h_i = 1$ m), $F = 1$ when concentration $A = 1$ and $\alpha_i = 1$. As the concentration (A) decreases below 0.8 the value of F goes exponentially to zero, suggesting the sea ice becomes free drift. This demonstrates that the design of Eq. (9) follows the free drift condition. The equation also implies that increasing or decreasing the value of α_i changes the HS/VS classification.

The limiting value of α_i for the sea ice field to be entirely classified as VS occurs when $F = 1$ for a lowest possible concentration of 0.8. This limiting value is given by:

$$\alpha_i^{vs} = \frac{e^4}{h_i}. \tag{12}$$

Similarly, the entire field is classified HS when $F = 1$ for the maximum concentration of $A = 1.0$. The corresponding α_i is given by:

$$\alpha_i^{hs} = \frac{1}{h_i}. \tag{13}$$

Using Eqs. (12) and (13), the limiting α_i is evaluated for the same 4 sea ice thicknesses as in Fig. 4. Since α_i is inversely proportional to h_i, the limiting classification of entire HS occurs for a maximum sea ice thickness $h_i (= 3.0$ m in our considered range of sea ice thicknesses) giving $\alpha_i^{hs} = 0.3$. Likewise, the limiting value for all VS classification occurs for a minimum thickness $h_i (= 0.5$ m) giving $\alpha_i^{vs} = 109.2$.

Acknowledging the uncertainty with α_i's value, in this study we estimate its value based on assumptions regarding the parameters in Eq. (11). We consider $P^* = 25$ kPa, $C = 20$ and $e_c = 2$ which are the original values in Hibler (1979)'s rheology. The sea ice–water friction coefficient (C_f) was assumed to be 5.5×10^{-3} as per McPhee (1980). The

maximum creep parameter Δ_o must be taken much smaller than typical strain-rates of sea ice for a good approximation of the plastic flow. Sea ice is seen to have strain rates from subdaily scale tidal and inertial forces of the order ranging from 10^{-6} to 10^{-7} s^{-1} (Kwok et al., 2003; Heil and Hibler, 2002). It is noted in Heil and Hibler (2002) that due to high-frequency motion like in case of tides, the sea ice deformation is also higher with higher divergence or strain rates. So, here, the larger of the two Δ_o is considered i.e. $\Delta_o = 10^{-6}$ s^{-1}.

U and L are the scaling parameters dependent on the physics of the problem. Since this involves sea ice–tide interaction, it serves as a criterion for the limit of sea ice drifting due to tidal movements. Hence, $U = 1$ m/s is assumed, representing a stronger tidal velocity. For L, the sea ice field on a continuum scale is considered, such a field is known to exist in shear and marginal zones when L is in the range of 10–15 km (Leppäranta, 2011a). Here, we are using GTSM which has a maximum grid cell size of up to 25 km in open oceans, down to a minimum of 2.5 km. Based on this, L is assumed to be 15 km, which, on average, would show sufficient resolution for GTSM grid cells and also satisfies the sea ice continuum criterion in shear zones. With these values, α_i evaluates to 1.2. This value is closer to the all HS limit, implying that in practice, there is more sea ice with HS than with VS.

Utilizing this value of α_i alongside the sea ice thickness and concentration, the value of F follows from Eq. (10). Implementing this value of F in Eq. (5) gives the classification of the sea ice field in HS and VS regions. The subsequent step involves modelling the sea ice dissipation from VS region with Eq. (6) and from the HS region with:

$$\nabla \cdot \boldsymbol{\sigma} = \eta(h_i, A)(\nabla^2 \boldsymbol{u}), \tag{14}$$

where sea ice horizontal shear viscosity, given by Eq. (8), can also be expressed as:

$$\eta = F \rho_w C_f U L^2, \tag{15}$$

where $U = 1$ m/s and $L = 15$ km.

3.3. Implementation of the parameterization

The new parameterization for sea ice-induced dissipation in ocean tide models, reliant on sea ice thickness and concentration, can be implemented in any ocean tide model as follows:

1. Obtain a suitable dataset with sea ice thickness and concentration fields for relevant regions with a sea-ice concentration larger than 0.8
2. Compute the value of the friction number F using Eq. (10) with $\alpha_i (= 1.2)$. Note that this scaling parameter may require calibration.
3. Classify the sea ice field into HS and VS regions based on the switching parameter λ given by Eq. (5).
4. Sea ice dissipation from the new classification (HS/VS) is then modelled in the shallow water equations of tide models by Eq. (3) with:

   • Dissipation from VS is modelled with Eq. (6) which is the same term as bottom frictional stress with different drag coefficient value.
   • Dissipation from HS is modelled with Eq. (14) which is the same as viscous diffusion from water but with a spatially varying sea ice shear viscosity computed from Eq. (15)

3.4. Validation

Here, we outline the validation steps to assess the performance of our parameterization. Initially, we provide details of the validation for the HS/VS classification, followed by the steps undertaken to assess the performance of our method in comparison to altimetry and tide gauge datasets.

The initial step involves obtaining an HS/VS classification of the sea ice field from Section 2.1. Additionally, we consider another classification of HS/VS by assuming $\alpha_i = 0.7$, chosen to result in a classification with a predominantly large HS region and minimal VS region coverage. Modifying $\alpha_i(= 0.7)$ equates to adjusting the maximum creep parameters Δ_o from 1×10^{-6} to 1.64×10^{-6} in the Eq. (11), altering the sea ice shear limits by modifying sea ice viscosity and thereby expanding the horizontal shear region. Using these two values of α_i, two sets of sea ice field classifications are obtained, denoted as *Exp HS_VS_1.2* for $\alpha_i = 1.2$ and *Exp HS_VS_0.7* for $\alpha_i = 0.7$ representing the two experiments.

Another classification, termed *Ex All_VS*, is similar to the current state-of-the-art method (Cancet et al., 2018; Kleptsova and Pietrzak, 2018; Bij de Vaate et al., 2021) where the entire sea ice field is assumed to be landfast ice or VS. The HS/VS region distribution resulting from these classifications is compared to the distribution of landfast and drifting sea ice using a gridded dataset from the National Snow and Ice Data Center (NSIDC) (US National Ice Center, 2020). This dataset providing the landfast sea ice and total sea ice concentration data is based on the National Ice Center (NIC) charts derived from manual analysis of various satellite images. This dataset will be referred to as *NSIDC* in the paper.

These classifications are implemented in GTSM with their corresponding dissipation characteristics. Model simulations are conducted for three settings: Exp All_VS, Exp HS_VS_1.2 and Exp HS_VS_0.7 for March and September months of the years 2012, 2017 and 2019, with a 7-day spin-up period. Water levels from the model simulation are used to compute M_2 amplitude and phase for March and September through tidal analysis with UTide (Codiga, 2011) using the major tides; K_1, O_1, Q_1, P_1, N_2, M_2 and S_2, consistent with the altimetry product (Section 2.2). The seasonal modulation of the M_2 tide is then evaluated as March–September differences in M_2 amplitude and phase.

Seasonal modulation from the model is compared to the altimeter- and TG-derived observations (Sections 2.2 and 2.3). The altimeter-derived seasonal modulation serves as an average over the data years (2010–2019). In contrast, the CHS tide gauge predictions of 2019 are based on harmonic analysis of past data collected by the tide gauge, lacking precise information of the year of collection. On the other hand, the seasonal modulation from tide gauges in Kulikov et al. (2020) data is computed from data collected over years ranging from 1981 to 2014 with each tide gauge operational during different periods of time. These details imply that the observations of altimeter- and TG-derived modulations are not ideal for model comparisons over the Arctic but having reliable, accurate and sufficiently long datasets over the entire Arctic is a challenge.

To address this to an extent, model simulations were performed for the two extreme years (2012 and 2017) and average (2019) of sea ice cover, allowing an assessment of the range of seasonal modulation of tides from the model results and aiding in attributing discrepancies between observed- and model-derived seasonal modulation.

The parameterization is validated by doing qualitative and quantitative comparisons between model results and observations. For the altimetry dataset, a qualitative comparison presents the seasonal modulation of the M_2 amplitude and phase for both observations and model results. Quantitative comparison faces challenges due to significant variability in altimeter-derived data, as noted in Section 2.2. To reduce this variability, a coarser grid of resolution $875\,\text{km} \times 875\,\text{km}$ is considered where the values at a grid cell are the median of all the observations/model results in that particular grid cell. A Pearson correlation coefficient is calculated between observed and model values on this coarser grid. Due to large variability, a *p*-value is also computed with the null hypothesis that the distribution underlying the samples is uncorrelated and normally distributed. A *p*-value below 0.05 is assumed to indicate a statistically significant correlation. For tide gauges, the qualitative comparison is similar to the altimeter-derived product, whereas quantitative comparison involves calculating the median of the difference between observations and model results across various years.

4. Results and discussion

4.1. Sea ice field classification for 2019

The gridded dataset from the NSIDC provides weekly outputs of landfast sea ice and total sea ice concentration. We consider the data from around mid-month as a representation of the mean for that month. The sea ice fields on March 21, 2019, and September 19, 2019, are shown (Figs. 5(a) and 5(b)) with concentrations larger than 0.8, displaying the distribution of landfast and total sea ice. It is observed that in September (Fig. 5(b); summer), the sea ice cover is significantly reduced with no landfast sea ice present in the dataset, in contrast to March (Fig. 5(a); winter). This loss in landfast sea ice during summer periods since 2018 is also noted by Li et al. (2020). For landfast ice, the March extent is around 10% of the total sea ice extent.

The HS/VS classifications from Exp HS_VS_1.2 and Exp HS_VS_0.7 for the sea ice field of 2019 are shown in Fig. 6. Similar figures showing classifications (Exp HS_VS_1.2 and Exp HS_VS_0.7) for the years 2012 and 2017 are available in Appendix C.

With Exp HS_VS_1.2, it is seen that for March (Fig. 6(a)), approximately 30% of the sea ice field is classified as VS, which is significantly larger compared to the landfast ice coverage (10%, Fig. 5(a)). The larger landfast ice regions, such as the Canadian Archipelago, the East Siberian Sea, and the Laptev Sea, are also identified as part of the VS regions, along with other areas in Hudson Bay and the Central Arctic. On the other hand, the HS classification for March primarily encompasses regions with strong tidal velocities like Ungava Bay, Hudson Strait, and near the Kara Sea, as well as along the sea ice edge where horizontal shear is expected due to the drifting nature of the sea ice surrounded by ocean. For September (Fig. 6(b)), a small region ($\sim$ 7% of the total) north of Greenland is classified as VS, while the remaining Central Arctic region and parts of the Canadian Archipelago are classified as HS, in contrast to the absence of landfast sea ice in September (Fig. 5(b)). This HS/VS classification validates the physical notion that regions within the drifting sea ice, possessing strong internal stresses, can remain almost stationary under tidal influences, resulting in vertical shear on tides.

In comparison, Exp HS_VS_0.7 for March (Fig. 6(c)) shows approximately 5% of the sea ice field as VS, mainly in the central Arctic north of the Canadian Arctic archipelago and Greenland. As expected with the choice of α_i, this VS region is minimal compared to the HS region, indicating that much of the sea ice field behaves as drifting sea ice with horizontal shear. The VS region is considerably smaller than the landfast ice cover for March (Fig. 5(a)). Likewise, for September (Fig. 6(d)), there is (almost) no VS region ($\sim$ 1–2%) similar to absence of landfast sea ice cover (Fig. 5(b)). Here again, it is seen that the HS classification is around the sea ice edge while the central the sea ice field with compact and large internal stresses is classified as VS due to the high viscosity of the ice field.

It should be noted that the landfast ice coverage is not a mean for that month, but the mean is expected to be within $\pm 2\%$ of the current distribution, as there are not significant variations within a month. The proportions of the HS/VS regions for March in both classifications exceed this range, and for September, there is no landfast ice. Thus, the discussion remains valid even if a mean landfast ice coverage were available. Currently, no dataset provides a monthly mean landfast ice coverage.

4.2. Comparing model-derived and observation-derived seasonal modulation

4.2.1. Results-altimetry dataset

The model-derived and altimetry-derived March–September differences in the amplitude and phase of the M_2 tide for the year 2019 are shown in Fig. 7. The plots obtained for the years 2012 and 2017 are shown in Appendix D.1.

(a) March 2019
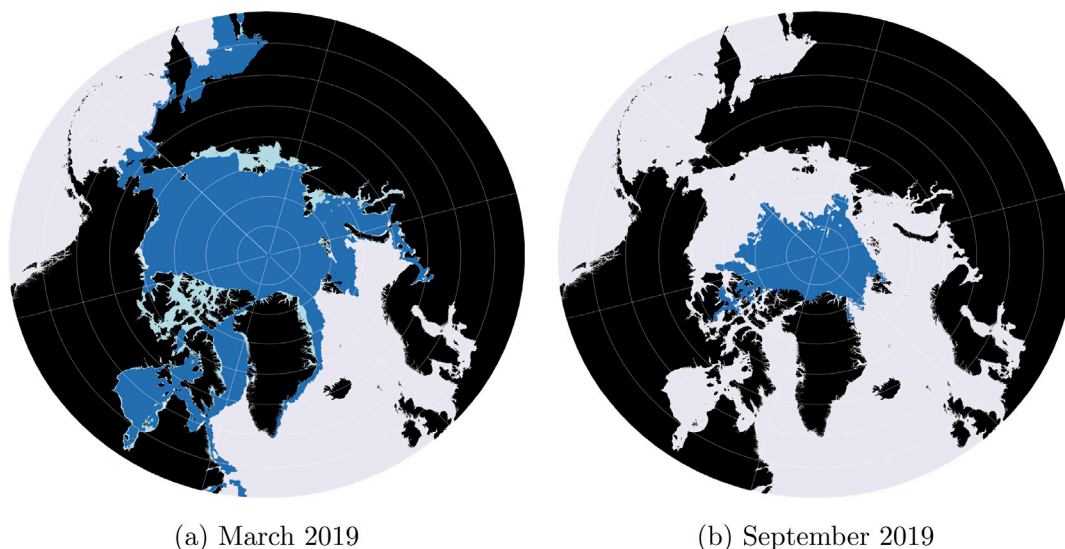
(b) September 2019

Fig. 5. Sea ice field for March and September 2019 obtained from NSIDC dataset. The sub-figures (Figs. 5(a) and 5(b)) show the traditional sub-division of landfast sea ice (light blue) from the remaining sea ice (dark blue) obtained from NSIDC. Note that only the sea ice field with concentration > 0.8 is considered here.

Table 1
Pearson correlation (R) and corresponding *P*-value for the plots in Fig. 8. The mean represents the mean of the values of the 3 years for that respective statistic with the green value denoting the model run with highest correlation in amplitude differences.

	Amplitude						Phase					
	Exp All_VS		Exp HS_VS_1.2		Exp HS_VS_0.7		Exp All_VS		Exp HS_VS_1.2		Exp HS_VS_0.7	
	R	P-value	R	P-value	R	P-value	R	P-value	R	P-value	R	P-value
2012	0.42	0.04	0.55	0.005	0.65	0.001	−0.002	0.99	−0.04	0.85	0.28	0.20
2017	0.45	0.03	0.58	0.003	0.60	0.002	−0.19	0.40	0.11	0.62	0.30	0.18
2019	0.47	0.02	0.52	0.009	0.60	0.002	0.032	0.88	0.24	0.28	0.38	0.079
Mean	0.45	0.03	0.56	0.006	0.62	0.001	−0.05	0.76	0.10	0.59	0.32	0.15

Fig. 8 displays the scatter plots of the altimeter-derived March–September amplitude and phase differences compared to their model-derived counterparts for the three years and each classification. The scatter plots are generated using the values on the coarser grid, and the map showing the median values for observations and model results is available in Appendix D.1. The resulting correlation coefficients and p-values are in Table 1.

Amplitude modulations are minimal in the Central Arctic and radiate outward to the Canadian and Russian Arctic sides. A strong seasonal modulation of up to ∼ ±0.25 m in the altimeter-derived estimates (Fig. 7(a)) is observed for several regions in the Hudson Bay, Hudson Strait, Frobesius Bay, Canadian Archipelago, White Sea and Kara Sea. Positive modulations are evident in the western part of Hudson Bay, Ungava and Frobesius Bay, White Sea, Laptev Sea, and west and east of Greenland in Baffin Bay, Labrador Sea, and near Svalbard. Negative modulations are noted in the eastern part of Hudson Bay, Canadian Archipelago, Barents Sea, Kara Sea, East Siberian Sea, and parts of the Chukchi Sea and Sea of Okhotsk. In the Central Arctic, the amplitude modulations are very low (around 2–3 mm), as expected due to the low tidal amplitudes in this region.

In comparison, the amplitude modulations with Exp All_VS for the year 2019 (Fig. 7(a)) exhibit much stronger seasonal modulation, up to approximately ±0.7 m. The distribution of positive and negative modulation appears smoother compared to the altimeter-derived estimates in the region. The areas of positive and negative distribution largely align with the altimeter-derived estimates, with a few exceptions. These exceptions include the western Hudson Bay and Strait, Frobesius Bay, Ungava Bay, and the Laptev Sea, where negative modulation is observed, and the southern Barents Sea, which exhibits positive modulation. Moreover, the Central Arctic, Chukchi Sea, and Sea of Okhotsk show almost zero modulation. A quantitative comparison using scatter plots reveals that only points around 0 amplitude modulation lie on the $y = x$ line (dotted line in the figure),

while the remaining points are scattered with no visible linear trend. This observation is supported by the resulting correlation coefficients, which average approximately 0.45 (Fig. 8). Furthermore, the amplitude modulation remains consistent across different years (2012, 2017, and 2019), except for four points in the plot.

The model-derived amplitude modulations with Exp HS_VS_1.2 for the year 2019 (Fig. 7(a)) also exhibit strong seasonal modulation, up to approximately ±0.4 m, albeit lower than Exp All_VS. The positive–negative distribution is very similar to the Exp All_VS case, except for a section of Hudson Bay and Frobesius Bay, where positive modulation is noted in Exp HS_VS_1.2. Additionally, the negative modulation in the Chukchi Sea and the southern region of Barents Sea diverges from Exp All_VS. The scatter plot (Fig. 8(b)) for this case similarly shows points only around 0 lying on the $y = x$ line, but exhibits a better linear trend compared to Exp All_VS. The average correlation coefficient between years is 0.55 (Table 1). Here, the scatter plot reveals varying amplitude modulations within different years, primarily for points distant from the $y = x$ line.

Lastly, the model-derived estimates for amplitude modulation with Exp HS_VS_0.7 for the year 2019 (Fig. 7(a)) display a lower seasonal modulation (up to approximately ±0.3 m) compared to the other two simulations but exceed the altimeter-derived estimates. The distribution of positive and negative modulation closely resembles Exp HS_VS_1.2, except for Frobesius Bay and some areas of Hudson Bay. In this region, Exp HS_VS_0.7 shows a broader spread of positive modulations compared to Exp HS_VS_1.2 and aligns with the altimetry-derived estimates. The scatter plots (Fig. 8(c)) includes points on the line $y = x$ that are not close to 0 and exhibit better linear trends compared to the other two simulations, with an average correlation coefficient of 0.6 (Table 1) between years. Moreover, amplitude modulations vary between years for nearly all points.

The variations in amplitude modulation for the results Exp HS_VS_0.7 and Exp HS_VS_1.2 between years indicate that modulations on the

(a) March 2019 (Exp HS_VS_1.2)

(b) September 2019 (Exp HS_VS_1.2)

(c) March 2019 (Exp HS_VS_0.7)

(d) September 2019 (Exp HS_VS_0.7)
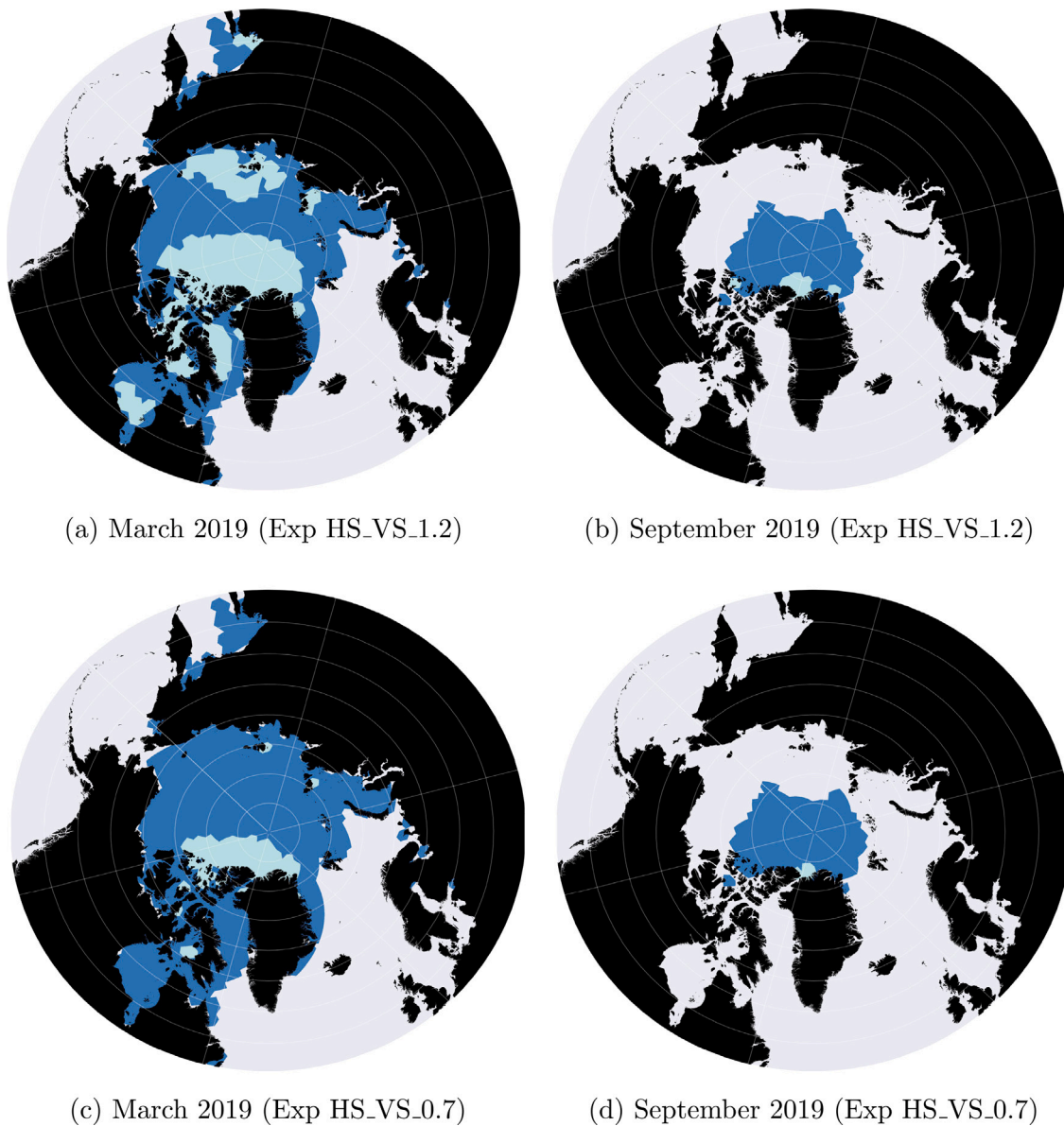
Fig. 6. HS (dark blue) and VS (light blue) classification of the sea ice field for March and September 2019 with the sea ice field obtained from Copernicus Marine Service (2019). The sub-figures show HS/VS classification based on two α_i values for the same the sea ice field. Exp HS_VS_1.2 is with $\alpha_i = 1.2$ and Exp HS_VS_0.7 is with $\alpha_i = 0.7$. Note that only the sea ice field with concentration > 0.8 is considered here.

Canadian Arctic side are larger in 2017 than in 2012, with 2019 serving as the median between them. Conversely, on the Russian Arctic side, 2017 has lower modulation, with 2012 exhibiting the largest among the three years. These modulations do not directly correlate with the fact that 2012 experienced the largest March–September differences in sea ice, while 2017 had the lowest.

Regarding phases, the hatched region in the phase plot of the altimeter-derived estimates (Fig. 7(b)), as mentioned by Bij de Vaate et al. (2021), signifies that these phase differences are deemed unreliable due to strong variability. Furthermore, the altimeter-derived estimates show considerable variability in phase modulation across the region, except for the Archipelago, where consistently positive differences are noted. Compared to altimeter-derived estimates, the model-derived estimates (Exp All_VS, Exp HS_VS_1.2, and Exp HS_VS_0.7, Fig. 7(b)) for the year 2019 demonstrate less variability in phase modulations. Consequently, the overall alignment between altimeter-derived phase modulations and model-derived modulations in scatter plots (Figs. 8(a), 8(b), 8(c)) is minimal, with insignificant correlation coefficients (Table 1). This lack of agreement persists across all years.

Among the three model-derived estimates, phase modulations from Exp All_VS (Fig. 7(b)) are negligible in many regions, except for a few areas on the Russian side of the Arctic and the southern part of the Labrador Sea. In contrast, Exp HS_VS_1.2 and Exp HS_VS_0.7 simulations present phase modulations throughout the entire region, with a comparatively lower proportion of areas showing negligible modulation. Additionally, the large phase differences in the central Arctic across all model simulations can be disregarded as artifacts or uncertainties, given the low amplitudes in the region near the North Pole.

4.2.2. Results-tide gauge dataset

The comparison with TG-derived March–September differences in amplitude and phase for the year 2019 is shown in Fig. 9. The results for the remaining years are provided in Appendix D.2.

Fig. 10 displays the TG-derived and model-derived (Exp All_VS, Exp HS_VS_1.2, and Exp HS_VS_0.7) estimates of amplitude and phase modulations for all the years, with the tide gauge names on the *x*-axis.
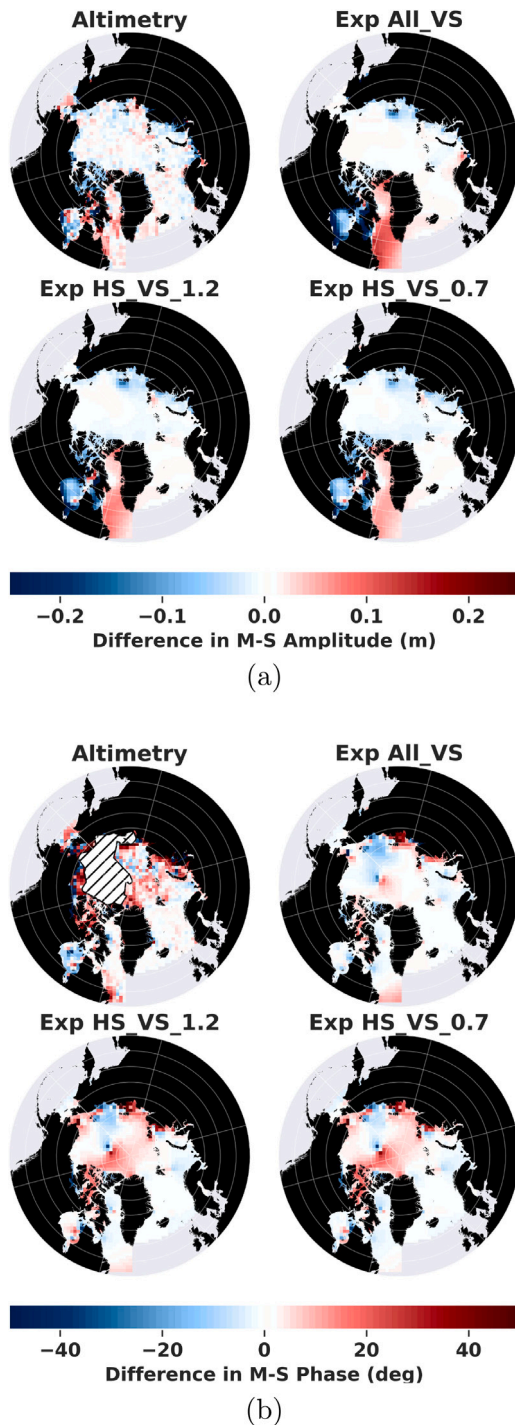
Fig. 7. Seasonal Modulation of M_2 tide quantified as March–September differences in amplitude and phases for the altimeter-derived product and the Exp All_VS, Exp HS_VS_1.2 and Exp HS_VS_0.7 runs for the year 2019. Differences in amplitude 7(a) and phase 7(b). Positive differences (red) denote that the March amplitude is larger/phase is leading than September, while negative differences (blue) denote the opposite.

TG-derived data indicate negative seasonal amplitude modulation across most CHS tide gauges, with the exception of those in the Labrador Sea (Fig. 9(a)). The tide gauge at La Grande Riviere in Hudson Bay exhibits the largest absolute amplitude modulation, recorded at 0.3 m. Similarly, in the Russian Arctic, negative modulations were observed, notably at the Wrangel gauge in the Chukchi Sea.

Comparisons with all three model simulations (Exp All_VS, Exp HS_VS_1.2, and Exp HS_VS_0.7) show consistent signs of seasonal amplitude modulation with the observed data, except at three tide gauges in

the Laptev and Chukchi Seas. Specifically, for the Wrangel tide gauge, model simulations suggest almost zero modulation, whereas observations indicate a modulation of −0.1 m. Among the model simulations, Exp All_VS exhibits larger amplitude modulations in absolute terms, while Exp HS_VS_1.2 and Exp HS_VS_0.7 generally align more closely with observed values. The median differences in amplitude modulation between observation-derived estimates and model-derived estimates (Fig. 10) indicate the best performance with Exp HS_VS_1.2 simulations and the poorest with Exp All_VS.

TG-derived phase modulation (Figs. 9(b) and 10) from CHS data, excluding a positive anomaly at Tuktoyaktuk (∼ 65°) in the Chukchi Sea, exhibit either negative or nearly zero seasonal modulation. Russian side gauges mostly show positive or neutral phase modulations, with a notable exception in the Laptev Sea displaying a small negative modulation (∼ −5°). The agreement between model-derived phase modulations for all simulations and observed values is poor, with deviations as high as 40° at four tide gauges.

Finally, variability among all the tide gauges between years of different model simulations is noted in Fig. 10. The Exp All_VS case exhibits a narrower range of amplitude and phase modulations between years for all tide gauges, except for La Grande Riviere, compared to the other two simulations. For La Grande Riviere, the range is wider than the other two, but only for amplitudes.

4.2.3. Discussion

The comparison between altimeter- and TG-derived versus model-derived March–September differences shows overall good agreement in terms of the signs (positive or negative) for the amplitude. However, in regions such as Ungava Bay, the Bering Sea, and some parts of the Laptev Sea, the direction of amplitude modulations does not align with the altimeter-derived values. A plausible explanation could be that the altimeter-derived seasonal modulation, as mentioned in Section 2.2, results from all seasonal forces (i.e. wind forcing, spatial density differences, stratification). On the other hand, the seasonal modulation of phases from altimeter- and TG-derived values is not captured very well by the model runs. In fact, model estimates of 4 tide gauges show deviations of around 40° from the observations.

Nevertheless, it should be noted that the observations are not without issues. The altimeter-derived values exhibit considerable variability and uncertainty. For tide gauges, we either lack knowledge of the year of data collection (CHS data) or the year of data collection differs from the model runs (Kulikov et al., 2020). For instance, this discrepancy could explain the poor performance observed at the Wrangel tide gauge, whose modulations are computed from data collected between 1981–1995. Model simulations show (almost) zero amplitude modulation for this tide gauge, while the observed modulation is −0.1 m. The period of 1981–1995 featured thicker and more extensive sea ice than the years in this study, which could have influenced the model-derived seasonal modulation at this tide gauge. With thicker ice conditions, the scaling parameter α_i would be higher than 1.2 due to a linear relationship between them, as this would increase the compressive strength, consequently leading to a larger VS region. Another issue with the tide gauge measurements is the presence of local seasonal forces. For instance, there are local forces like seasonal river discharges due to ice melting which could affect the observations or tide gauge damage due to winter sea ice conditions. Such issues were particularly noted for the tide gauge Churchill near the Hudson River (Ray, 2016).

The variations in sea ice cover can affect amplitude modulations far from their source, with no direct relationship to the variations. For instance, the March–September differences were maximum for 2012, yet the absolute amplitude modulations for 2012 were lower on the Canadian side of the Arctic than the 2017 modulations. Conversely, on the Russian Arctic side, absolute amplitude modulations for 2012 were larger than those in 2017.

Among all the types of model simulations, it is observed that Exp HS_VS_0.7 simulations (Fig. 9, Table 1) show the best overall agreement
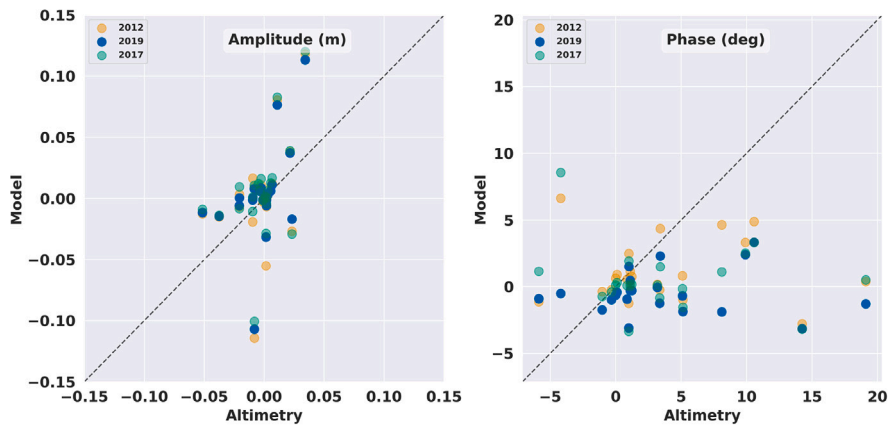
(a) Sea ice as Fixed
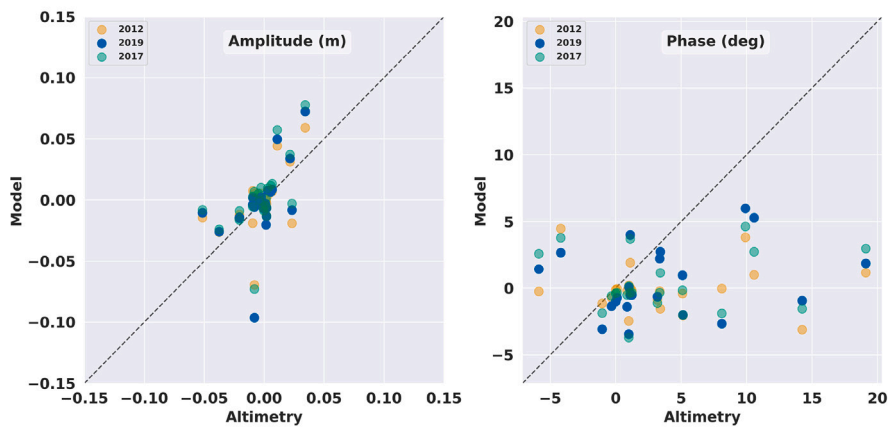
(b) Exp HS_VS_1.2
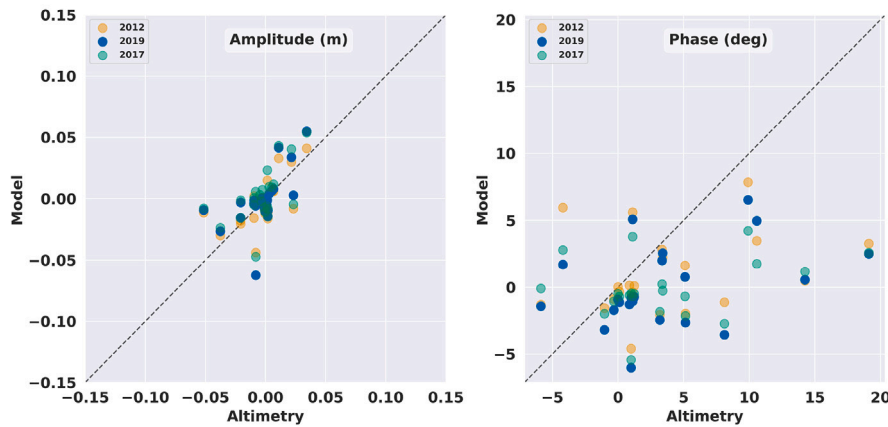
(c) Exp HS_VS_0.7

Fig. 8. Scatter plots showing a comparison between altimeter-derived seasonal modulation (*x*-axis) versus the seasonal modulation (March–September differences of M$_2$ constituent) from the 3 Model results (Exp All_VS, I and II) (*y*-axis). Each sub-figure corresponds to the respective model simulation with the sub-title denoting the name of the simulation and the amplitude and phase modulations are compared separately. The colour of the dots correspond to the year of the run. Note that each point corresponds to the value at the cell of the coarse grid and importantly, the phase differences of the cells lying in the hatched region (Fig. 7(b)) are removed from the plotting.

with the altimeter-derived values, while Exp HS_VS_1.2 simulations (Fig. 10) have the best overall agreement with the tide gauge results. The Exp All_VS case, which represents a current state-of-the-art in many tidal models, shows larger seasonal modulations of amplitude implying a larger dissipation from the sea ice on tides. This outcome is expected

since a landfast ice assumption represents an extreme dissipation condition at the ice–water interface. The Exp HS_VS_1.2 and Exp HS_VS_0.7 simulations, which are based on the new parameterization derived in this paper, exhibit comparatively lower amplitude modulations. Here, the drifting sea ice is treated separately with its own dissipation characteristics modelled through the HS region. Such dissipation, by virtue of

(a)
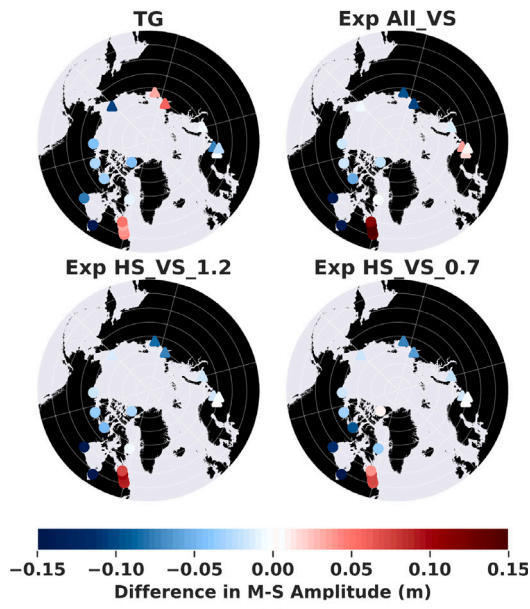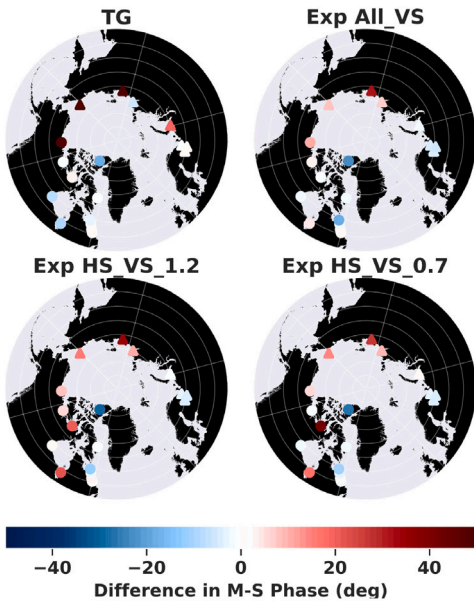
(a) Exp All_VS

(b)

Fig. 9. Seasonal Modulation of M$_2$ tide quantified as March–September differences in amplitude and phases for the TG-derived product and the 3 model runs (Exp All_VS, Exp HS_VS_1.2 and Exp HS_VS_0.7) for the year 2019. Differences in amplitude 9(a) and phase 9(b). Positive differences (red) denote that the March amplitude is larger/phase is leading than September, while negative differences (blue) denote the opposite.

its construction (friction number formulation) in the parameterization, is lower than the dissipation from landfast ice. This can be verified in the results, as Exp HS_VS_0.7 has lower amplitude modulation than Exp HS_VS_1.2, while it has a larger HS area than Exp HS_VS_1.2.

Although some tidal models can change the ice–water drag coefficient in the landfast ice assumption to alleviate (to some extent) the problem of strong dissipation from the landfast ice assumption. In fact, Kleptsova and Pietrzak (2018) proposed a solution wherein the drag coefficient varied with ice concentration. Nonetheless, these multiple approaches still do not account for drifting sea ice and its resulting velocity gradients, which can lead to different dissipation characteristics. Our new parameterization is equipped to deal with
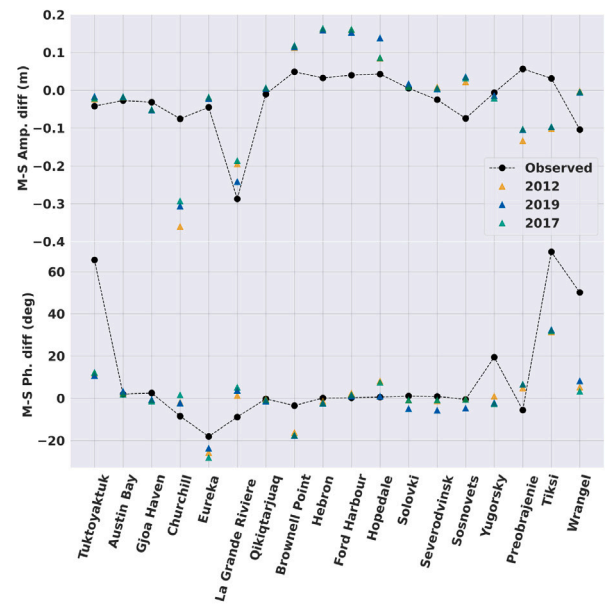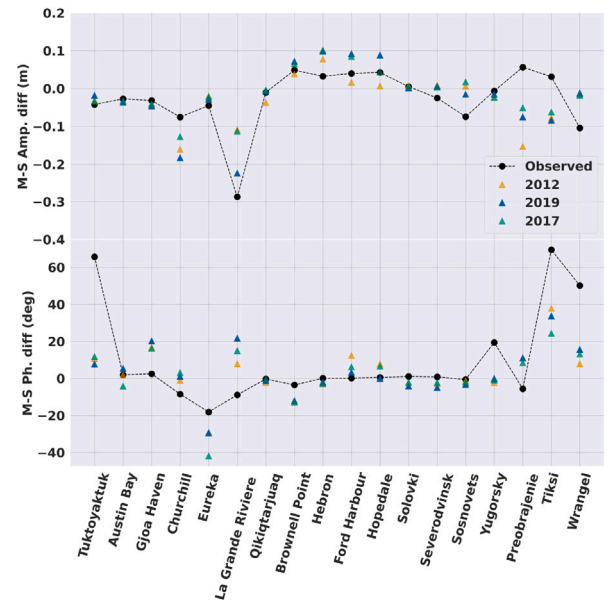
(b) Exp HS_VS_1.2

Fig. 10. Seasonal modulation per tide gauge (on *x*-axis) with observations in black dots connected by dotted lines. The model results are shown by triangles with different colours corresponding to a particular year. The tide gauges are arranged on the *x*-axis in order of increasing longitude (going anti-clockwise) starting from Tuktoyaktuk (Lon 133°W) to Wrangel (Lon 178°E). The first 11 tide gauges on the *x*-axis are from the CHS data and the next 7 are from Kulikov et al. (2020). The first 3 sub-figure captions denote the type of model simulation among Exp All_VS, Exp HS_VS_1.2 and Exp HS_VS_0.7. The last sub-figure is the median of difference between model and observed values computed over 3 years. The colours in this sub-figure correspond to the three types of model runs. A value closer to zero indicates better agreement of the model simulation to the observed value.

such dissipation characteristics by modelling the dissipation with a diffusion term and sea ice viscosity. This diffusion term will lead to larger dissipation when sea ice velocity gradients are expected to be larger, for example, in regions like the Hudson Strait and Frobesius Bay.

Furthermore, the dissipation is also designed to handle the spatial and temporal variability of sea ice thickness (h_i) and concentration (A) through the value of sea ice viscosity and the classification in

(c) Exp HS_VS_0.7

(d) Median of differences

Fig. 10. (*continued*).

This value could further be fine-tuned through calibration using data assimilation principles to improve the HS/VS classification and the resulting model outcomes. Secondly, the ice–water drag coefficient C_f used here, and in most other studies, is obtained from McPhee (1980). This coefficient is larger for recent first-year ice in the Arctic than for the experiments conducted in 1978 (McPhee, 2017). Moreover, the value of this drag coefficient is also known to exhibit a seasonal pattern (Brenner et al., 2021). Therefore, further research into better representation of drag coefficients will lead to more accurate dissipation values. Finally, the parameter λ for simplicity, is assumed to be a binary parameter switching between the two regions, i.e., HS/VS. However, a smooth transitioning parameter between the two regions (e.g., a sigmoid function) could provide better modelling, potentially altering the HS/VS classification and, thus, the results. Nonetheless, the current assumptions regarding these parameters represent a first step, and the values chosen here are based on tidal characteristics and a simplistic representation.

5. Summary and conclusions

The impact of sea ice decline on global tides is still a topic of ongoing research. To study such an impact global hydrodynamic tidal models should include, in their modelling, the effect of sea ice induced dissipation on tides. Most models either ignore this effect or model it by assuming a monthly mean sea ice cover which is fixed i.e. landfast ice.

Here, we propose a novel parameterization to model sea ice-induced dissipation on tides, distinguishing between landfast and drifting sea ice through Horizontal Shear (HS) and Vertical Shear (VS) regions, determined by a Friction Number (F). This number incorporates sea ice thickness (h_i), concentration (A), and a scaling parameter (α_i). From the range of values of α_i two were selected based on tidal characteristics and the nature of HS/VS regions, leading to classifications Exp HS_VS_1.2 and Exp HS_VS_0.7, showcased for March and September 2019 in Fig. 6. This parameterization's efficacy was assessed within the Global Tide and Storm Surge Model (GTSM) by comparing three simulations–Exp All_VS, Exp HS_VS_1.2, and Exp HS_VS_0.7—to altimeter- and TG-derived observations, focusing on the seasonal modulation of the M_2 tide. The Exp All_VS simulation assumes the entire sea ice field as landfast which is the current state-of-the-art in many tidal models.

Overall, the simulation results from the Exp HS_VS_1.2 and Exp HS_VS_0.7 experiments demonstrate better agreement with observations than the Exp All_VS simulations, which exhibited larger seasonal modulation indicating higher sea ice-tidal dissipation. This discrepancy is expected because the Exp All_VS approach does not distinctly treat drifting sea ice, and its assumption of landfast sea ice implies extremum in dissipation. Furthermore, the new parameterization accounts for the spatial and temporal distribution of sea ice thickness and concentration, making it apt for studying the implications of recent decline in sea ice thickness. It is also notable that changes in sea ice can influence tidal modulation (or tides) distantly from its source, with the relationship being non-linear.

However, this study is limited by the observational dataset. The altimetry-derived seasonal modulation represents an average over the data collection years (2010–2019), while the year of data collection for TG-derived modulation is either unknown or does not coincide with the model simulation years of 2012, 2017, and 2019. Ideally, a desirable dataset would encompass spatially distributed tidal water levels from tide gauges corresponding to the year of the model simulations, facilitating a more accurate comparison. The Canadian Hydrographic service is doing great work on this end, but on the Russian side of the Arctic there is still a lack of publicly available data. However, due to issues pointed out in Ray (2016) the tidal water levels from any such Arctic tide gauges should undergo a thorough quality check.

HS/VS regions. This inclusion of sea ice parameters helps in reducing dissipation when sea ice is thin and increasing dissipation for thicker sea ice. Given that such variability cannot be addressed with the simple assumption of landfast sea ice, it is observed that changes in sea ice cover between years does not have significant differences in seasonal modulation in Exp All_VS simulations. Our parameterization can deal with this variability making it suitable for studying the effects of sea ice decline on tides and thus, has a more accurate representation of sea ice–water physics than the simple landfast sea ice assumption.

Still, Exp HS_VS_1.2 and Exp HS_VS_0.7 model simulations, when compared against the observations used in this study, do not seem to exhibit very good accuracy. Apart from the fact that the observations have their own uncertainties, the parameterization developed here also incorporates some approximations and assumptions that can affect the model-derived results. Firstly, there is uncertainty in the scaling parameter (α_i) stemming from the uncertainty of the parameters in Eq. (11).

(a) March 2019

(b) September 2019

Fig. A.11. The sea ice field for March and September 2019 obtained from NSIDC dataset. The sub-figures (Figs. A.11(a) and A.11(b)) show the traditional sub-division of landfast ice (light blue) from the remaining sea ice (dark blue) obtained from NSIDC. Note that only the sea ice field with concentration > 0.8 is considered here.

In case such an observational dataset is available, it would also help in further research on improving the estimations of the uncertain parameters like the scaling parameter (α_i) and the drag coefficient (C_f) through calibration or tuning. Another approach to improve the estimation of the scaling parameter (α_i) is the utilization of a sea ice velocity dataset. Such a dataset can aid in estimation of HS/VS regions and thereby assist in refining the scaling parameter. However, this approach requires investigation due to the temporal scale mismatch between the tides and the daily to monthly scales of sea ice velocities in the datasets.

The results of this study should be viewed in the context of the challenges in obtaining an accurate representation of sea ice concentration and thickness and the limitations of the GLORYS model. Due to over estimation of sea ice thickness, the VS region is more, consequently providing larger dissipation. Ideally, a monthly averaged remote sensing-based product providing both sea ice thickness and concentration or an accurate model-based product is desirable.

Here, we used the seasonal modulation of the M_2 tide as a performance metric. However, other tidal constituents, such as S_2, O_1, and K_1, also experience seasonal modulation as noted in Wang and Bernier (2023). Seasonal modulation of these additional constituents could also serve as performance metrics, provided that suitable datasets are available.

We focused exclusively on Arctic sea ice, yet our parameterization can be extended to Antarctic sea ice, which is notably thinner due to the absence of multi-year ice and (almost) complete summer melt. This results in a lower ice–water drag coefficient for Antarctic sea ice—about 40% lower than Arctic averages (Schroeter and Sandery, 2022)—suggesting lower dissipation effects. Considering these differences, applying and investigating our parameterization for Antarctic sea ice could provide valuable insights.

In conclusion, this parameterization represents an initial step towards enhancing tidal models to incorporate sea ice dissipation effects on tides without necessitating coupling to a sea ice model. Such advancements promise a more realistic representation of sea ice in tidal models, aiding in the global analysis of the impacts of sea ice decline on tides and supporting coastal flood management strategies.

CRediT authorship contribution statement

Amey Vasulkar: Writing – review & editing, Writing – original draft, Visualization, Validation, Software, Resources, Project administration, Methodology, Investigation, Formal analysis, Data curation,

Conceptualization. **Martin Verlaan:** Writing – review & editing, Writing – original draft, Supervision, Methodology, Conceptualization. **Cornelis Slobbe:** Writing – review & editing, Writing – original draft, Supervision, Methodology, Investigation. **Mikhail Kulikov:** Writing – review & editing, Resources.

Declaration of competing interest

The authors declare that they have no known competing financial interests or personal relationships that could have appeared to influence the work reported in this paper.

Data availability

Data will be made available on request.

Appendix A. Comparing sea ice extent from GLORYS with NSIDC

The accuracy of the parameterization of the effect of sea ice developed here depends, among others, on the sea ice dataset providing the sea ice thickness and concentration. Currently, we used the dataset from Copernicus Marine Service (2019) which was a model derived reanalysis product. Here, we show the comparison of the sea ice cover from that product to the sea ice cover obtained from the NSIDC dataset which also gives the landfast ice cover. This product was also used previously to compare the area of HS/VS classification with landfast ice. The NSIDC product was also used in the landfast ice study of Bij de Vaate et al. (2021). The sea ice extent with concentrations larger than 0.8 is obtained from this dataset for the year 2019 (Fig. A.11).

This dataset does not have monthly mean data but an output every two weeks. Here, we consider the data for around mid of the respective

(a) March 2019
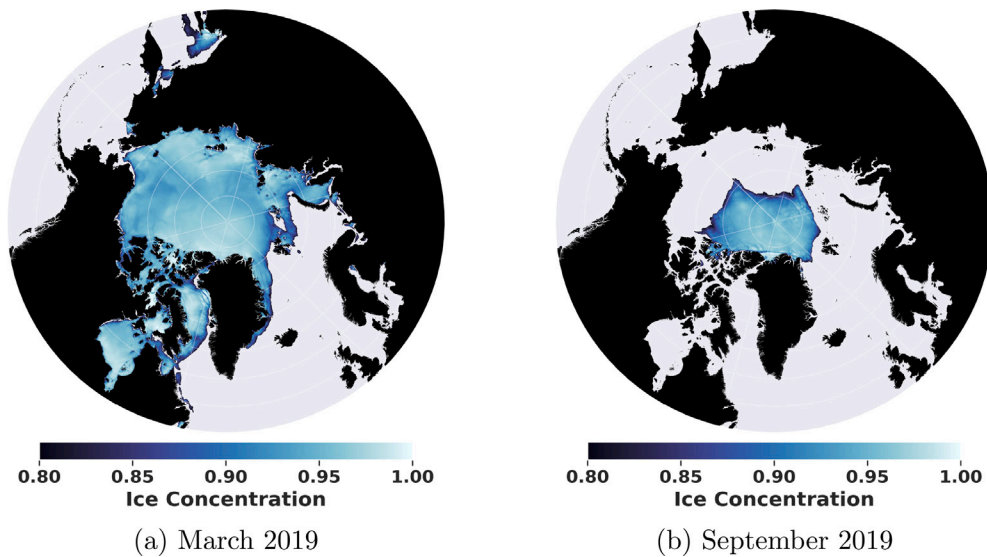
(b) September 2019

Fig. A.12. Sea ice concentration field with values larger than 0.8 for March and September 2019 obtained from a global ocean reanalysis product (Copernicus Marine Service, 2019). The sub-figures (Figs. 1(a) and 1(b)) show the March and September distribution.
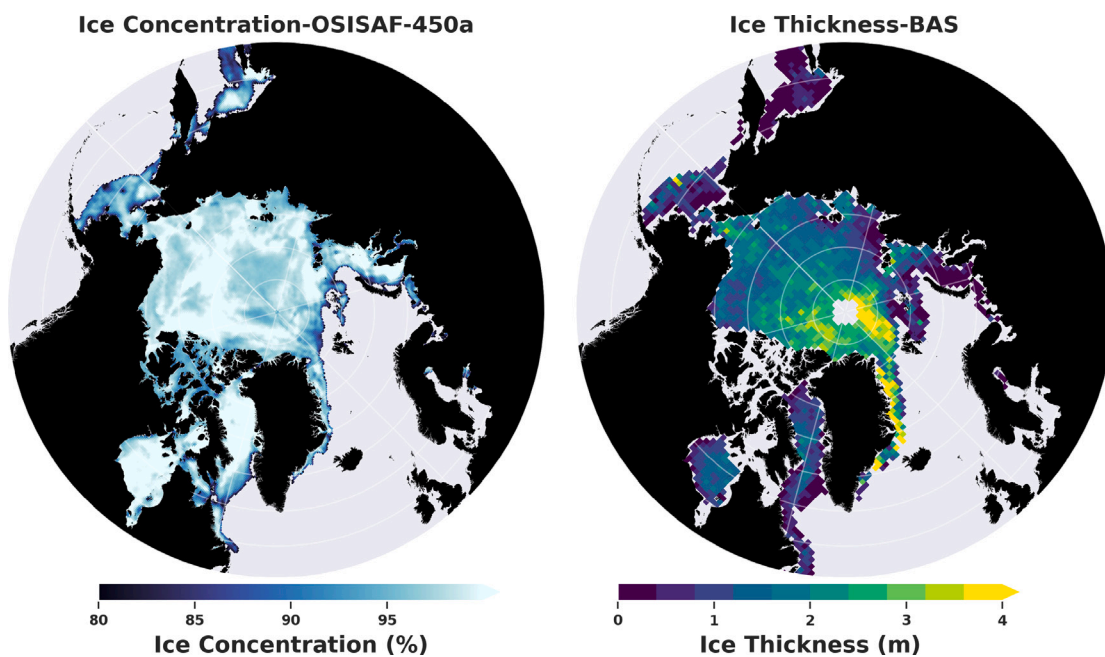
Fig. B.13. Sea ice concentration and thickness obtained from two different observation products for March 9, 2012. The concentration is derived from the OSISAF-450a product, while the sea ice thickness is from Landy et al. (2022), which evaluates thicknesses using CryoSat −2. BAS refers to the British Antarctic Survey as this product was released by them.

months and assumed that this data is a representation of the mean for that month. The sea ice field on March 21, 2019 and September 19, 2019 are shown (Figs. 5(a) and 5(b)) with concentrations larger than 0.8 and landfast (light blue) and total sea ice (dark blue) regions. It is seen that in September (Fig. A.11(b); summer) the sea ice cover is very low with no landfast sea ice in the dataset as compared to March (Fig. 5(a); winter) This is also noted in Li et al. (2020) that there is almost no landfast sea ice in the summer periods since 2018. Furthermore, this NSIDC landfast ice estimate will represent a physical lower bound of the VS region in our analysis. This can also give an idea of the value of the scaling parameter (α_i). However, it should be with a

caveat that these charts from NSIDC are produced by a manual analysis on satellite images. So the region of landfast ice might vary.

The monthly mean sea ice cover for March and September from Copernicus Marine Service (2019) is seen in Fig. A.12. On comparison, the sea ice cover from both the datasets have very similar coverage with some small discrepancies. The noted discrepancies off the coast of Japan, Bering Sea and southern Labrador Sea could be due to the fact that the Copernicus Marine Service (2019) dataset is a monthly mean where as NSIDC provides for a value at a particular day. Or possibly that the sea ice–ocean coupled models (including GLORYS used in the CMEMS product) often suffer from biases. For instance, the GLORYS

Ice Concentration-OSISAF-450a
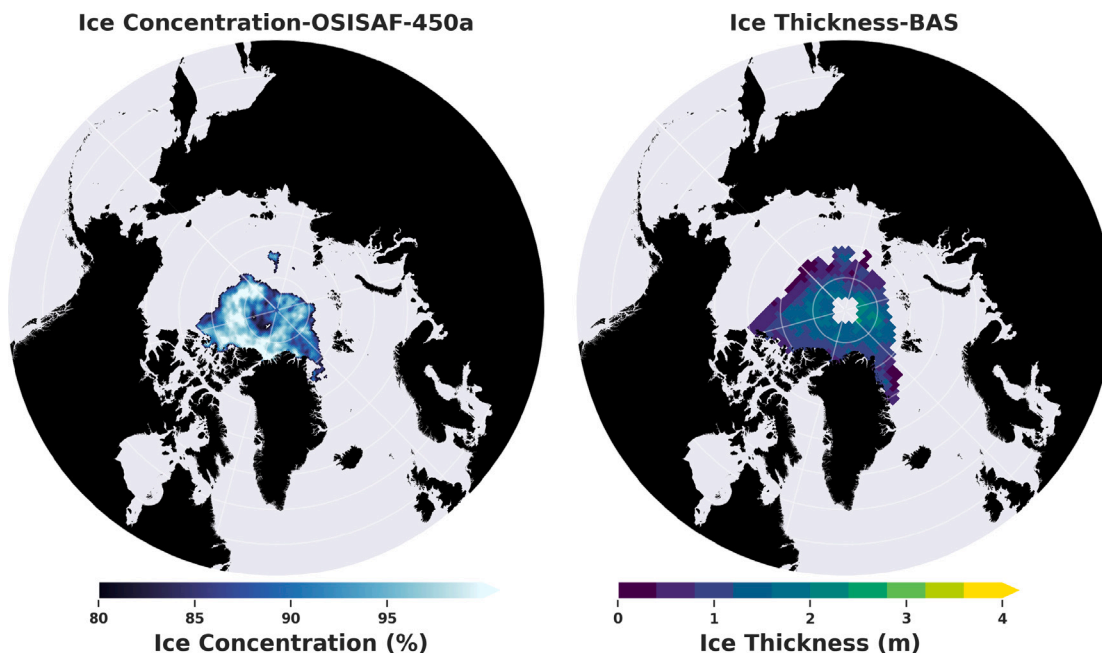
Ice Thickness-BAS

Fig. B.14. Sea ice concentration and sea ice thickness obtained from two different observation products for September 8, 2012. The concentration is obtained from OSISAF-450a product. The sea ice thickness is obtained from Landy et al. (2022) which evaluates thicknesses from CryoSat2. BAS refers to the British Antarctic Survey as this product was released by them.

Ice Concentration-OSI450a

Ice Thickness-CSMOS
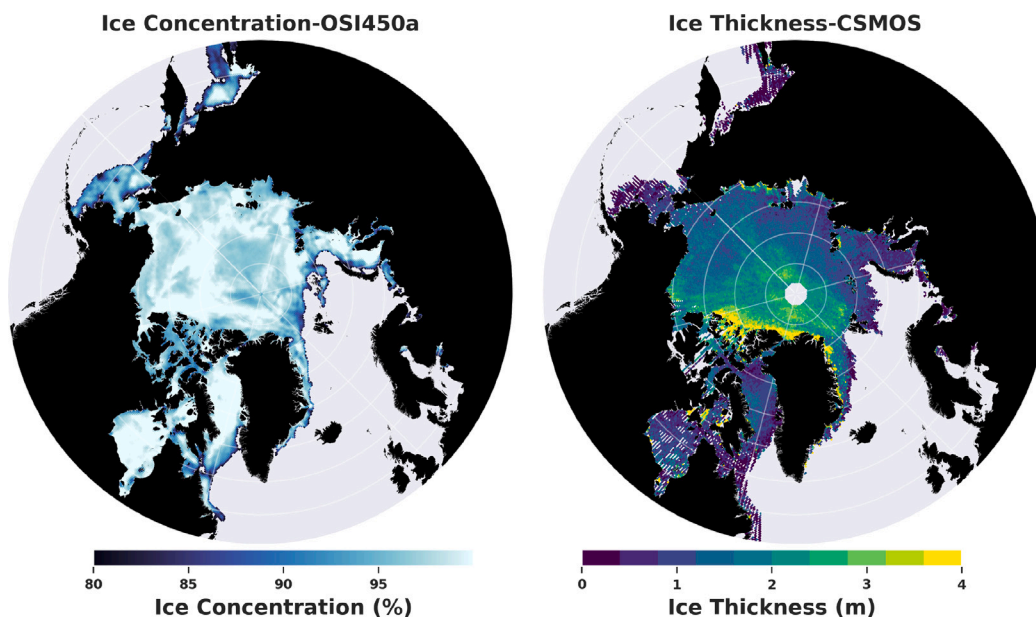
Fig. B.15. Sea ice concentration and sea ice thickness obtained from two different observation products for March 9, 2012. The concentration is obtained from the OSISAF-450a product. The sea ice thickness is obtained from the CS2SMOS product, which evaluates thicknesses from CryoSat −2 and SMOS and provides monthly averages.

model is known to have larger sea ice thicknesses than observed due to the underlying EVP rheology.

Appendix B. Comparing sea ice parameters from remote sensing products

We compared the concentration and thickness of sea ice from different remote sensing products to evaluate their efficacy. Sea ice concentration data were obtained from EUMETSAT Ocean and Facility (2022) (OSISAF-450a product), and sea ice thickness data were

obtained from Landy et al. (2022). We compared the data output for March 9, 2012, and September 8, 2012, from both datasets, as these were the matching dates we could find in our simulation years of 2012, 2017, and 2019. No monthly averages from these products were available.

From the sea ice thickness and concentration plots (Fig. B.13), data gaps were observed in the sea ice thickness product, particularly in the Canadian Archipelago, Hudson Bay, and Hudson Strait. These regions are significant in the context of sea ice-induced dissipation. The

(a) March 2012 (Exp HS_VS_1.2)

(b) September 2012 (Exp HS_VS_1.2)

(c) March 2012 (Exp HS_VS_0.7)

(d) September 2012 (Exp HS_VS_0.7)
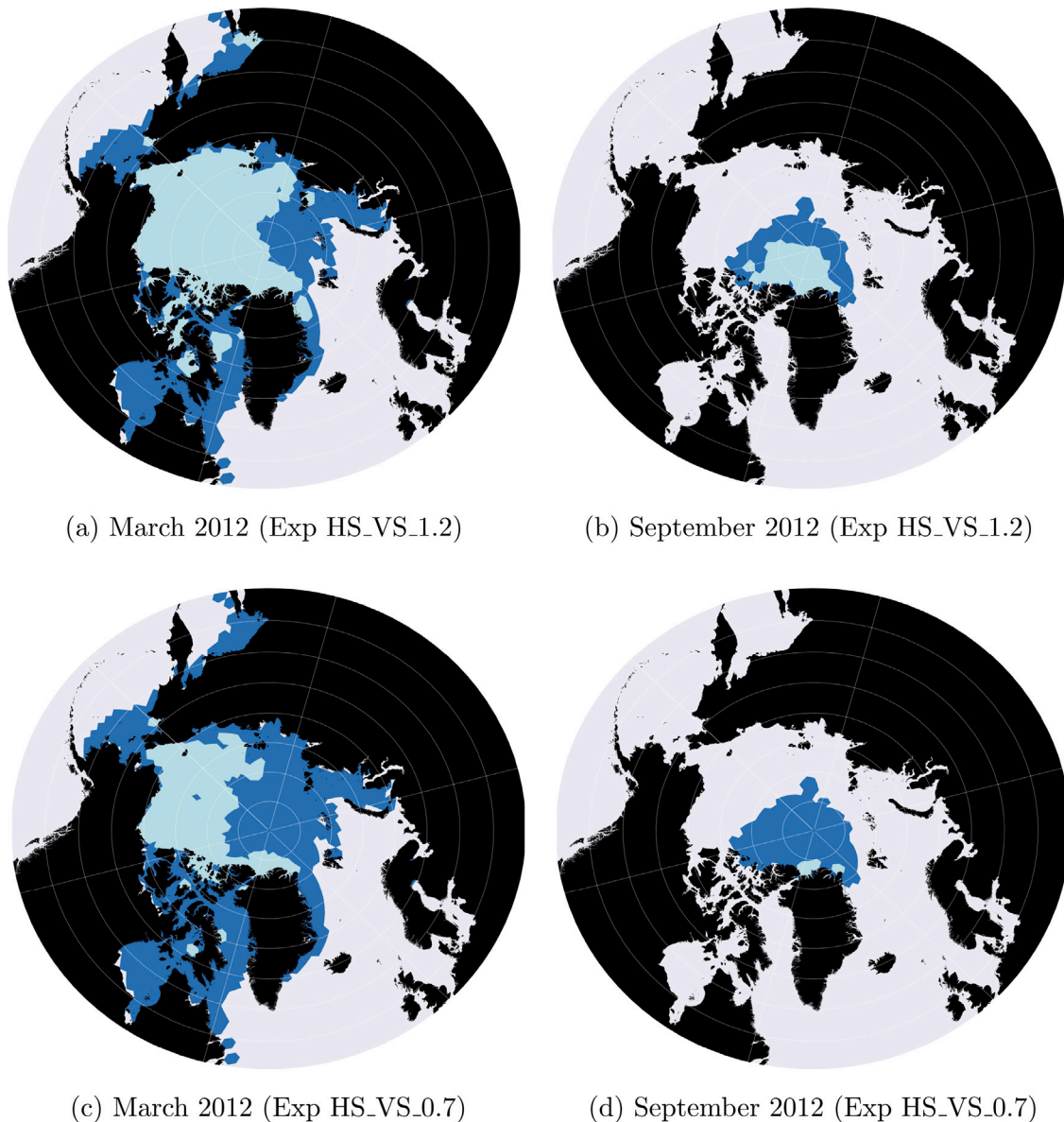
Fig. C.16. HS (dark blue) and VS (light blue) classification of the sea ice field for March and September 2012 with the sea ice field obtained from Copernicus Marine Service (2019). The sub-figures show HS/VS classification based on two α_i values for the same sea ice field. Exp HS_VS_1.2 is with $\alpha_i = 1.2$ and Exp HS_VS_0.7 is with $\alpha_i = 0.7$. Note that only the sea ice field with concentration > 0.8 is considered here.

comparison for September (summer) also revealed mismatches between the concentrations and thickness data (Fig. B.14).

Further comparisons were made with a sea ice thickness dataset from SMOS and CryoSat −2 provided by AWI (CS2SMOS product Ricker et al. (2017)). This dataset, available only for March, provided monthly averages.

The monthly average from CS2SMOS (Fig. B.15) when compared with the sea ice concentration on March 9, 2012 from OSISAF-450a showed that for the sea ice concentration from the Bering Sea, there was no corresponding sea ice thickness in the CS2SMOS product. Additionally, the thickness product missed some regions in the Canadian Archipelago.

This analysis highlights the potential data mismatches and spatio-temporal challenges associated with using remote sensing products. However, with improvements in remote sensing technologies, it is expected that future products will provide better quality data with the required spatio-temporal coverage, allowing for their direct use in place of model-based products in our new parameterization.

Appendix C. Sea ice classification results

The model runs were done for 3 years; 2012, 2017 and 2019 with the respective sea ice fields for those years. Here, we show the results from the Exp HS_VS_1.2 and Exp HS_VS_0.7 classification for
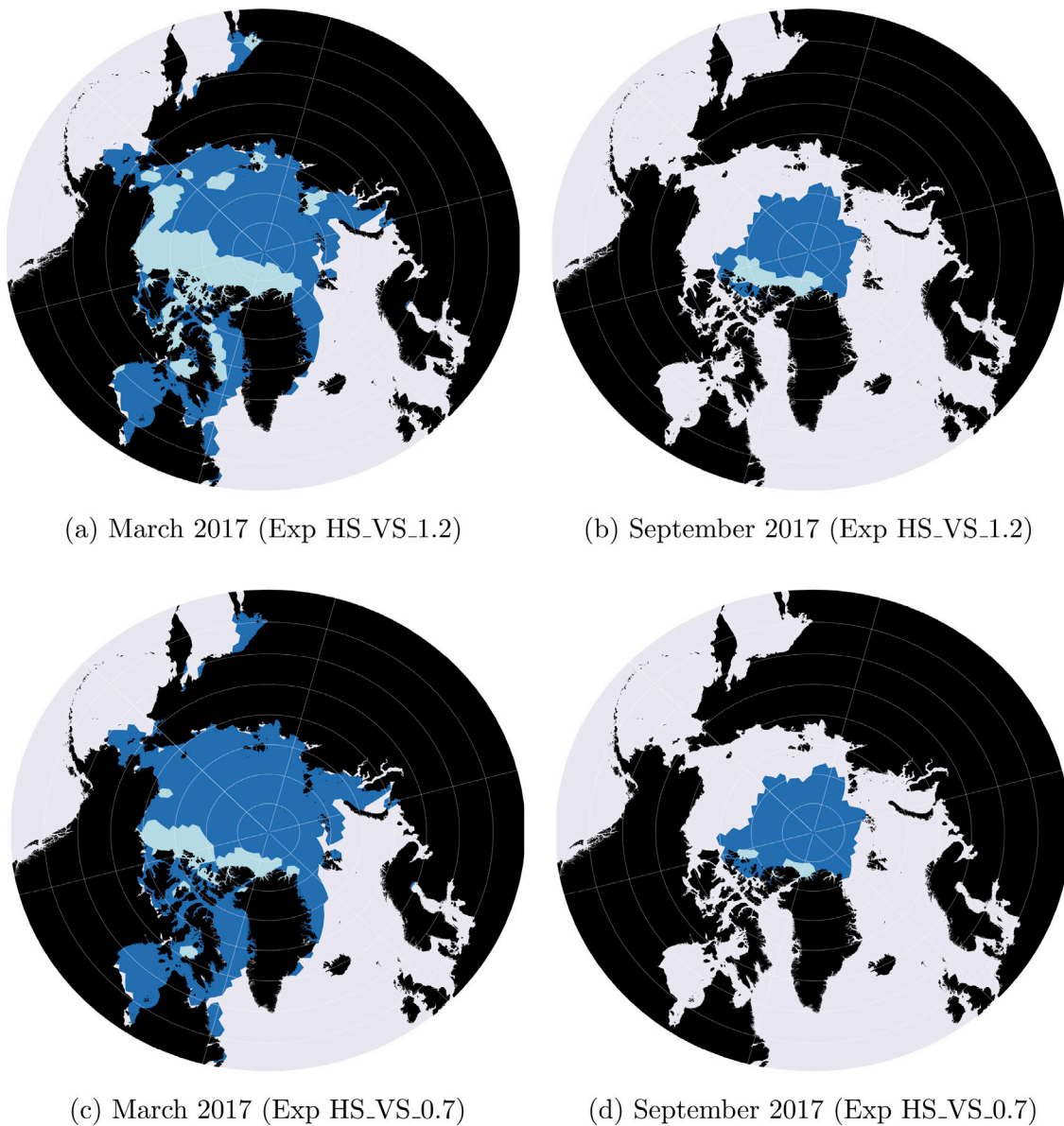
Fig. C.17. HS (dark blue) and VS (light blue) classification of the sea ice field for March and September 2017 with the sea ice field obtained from Copernicus Marine Service (2019). The sub-figures show HS/VS classification based on two α_i values for the same sea ice field. Exp HS_VS_1.2 is with $\alpha_i = 1.2$ and Exp HS_VS_0.7 is with $\alpha_i = 0.7$. Note that only the sea ice field with concentration > 0.8 is considered here.

the two months; March and September for the years 2012 and 2017. These years as mentioned previously, represent the maximum and minimum differences of the sea ice cover between March and September. Fig. C.16 shows the classification for 2012 while Fig. C.17 gives the classification for 2017.

Appendix D. Additional model results

D.1. Comparison with altimetry

The map of model-derived March–September differences in M_2 amplitude and phase at altimeter product locations for the years 2012 and 2017 are given in Figs. D.18 and D.19, respectively.

The altimetry data has noise which was reduced by first considering a coarser grid ($875\,\text{km} \times 875\,\text{km}$). Then, all the points from the altimetry product which were part of a particular grid cell were selected and a median of these points was computed. This median value was a representation of that grid cell/area of the region. The resulting values on the coarser grid was used to compute the correlation plots (Fig. 8). The coarse grid values of March–September differences for 2019 are shown here in Fig. D.20.

D.2. Comparison with tide gauges

The map of model-derived March–September differences in M_2 amplitude and phase at tide gauge locations for the years 2012 and 2017 are given in Figs. D.21 and D.22 respectively.

(a)

(b)
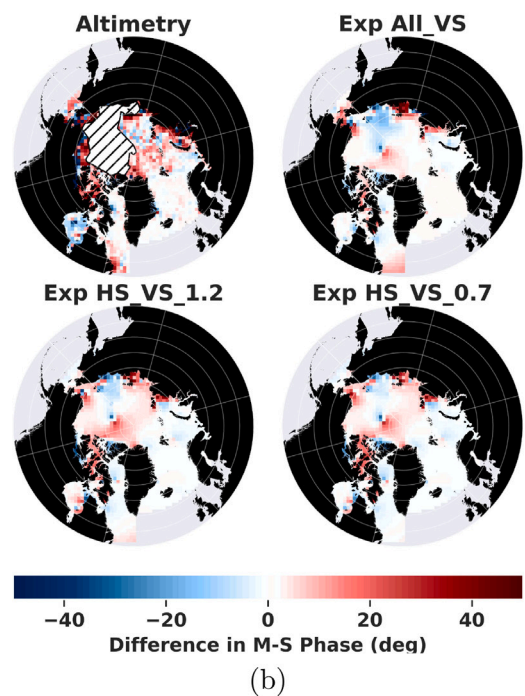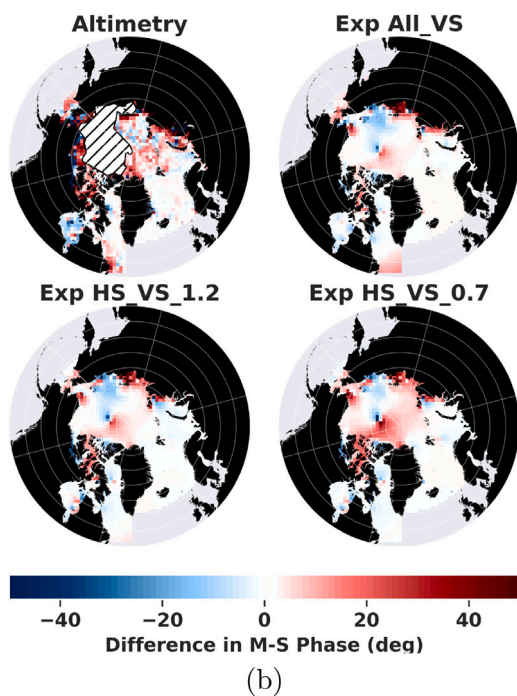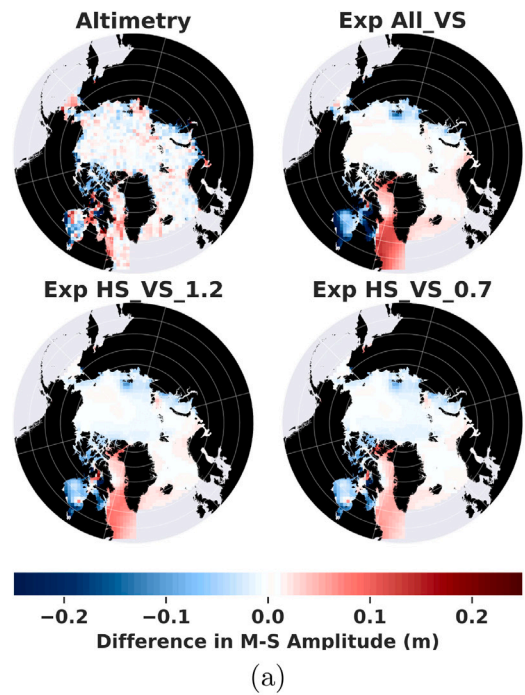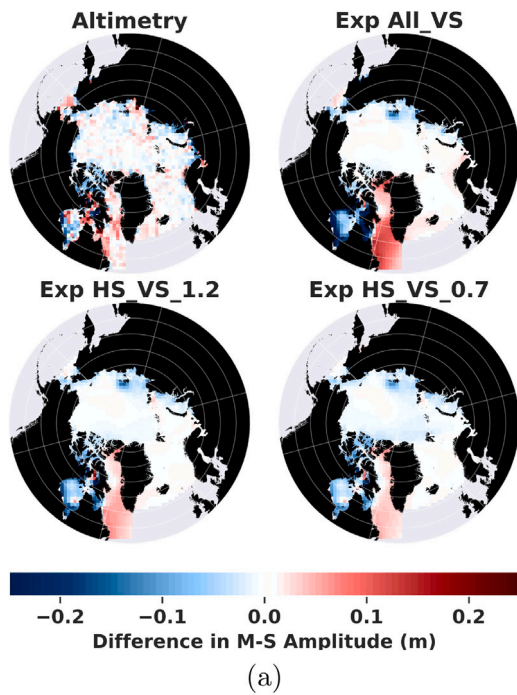
Fig. D.18. Seasonal Modulation of M_2 tide quantified as March–September differences in amplitude and phases for the altimeter-derived product and the Exp All_VS, Exp HS_VS_1.2 and Exp HS_VS_0.7 runs for the year 2012. Differences in amplitude D.18(a) and phase D.18(b). The positive differences (red) denote that the March amplitude is larger/phase is leading than September, while negative differences (blue) denote the opposite.

(a)

(b)

Fig. D.19. Seasonal Modulation of M_2 tide quantified as March–September differences in amplitude and phases for the altimeter-derived product and the Exp All_VS, Exp HS_VS_1.2 and Exp HS_VS_0.7 runs for the year 2017. Differences in amplitude D.19(a) and phase D.19(b). The positive differences (red) denote that the March amplitude is larger/phase is leading than September, while negative differences (blue) denote the opposite.
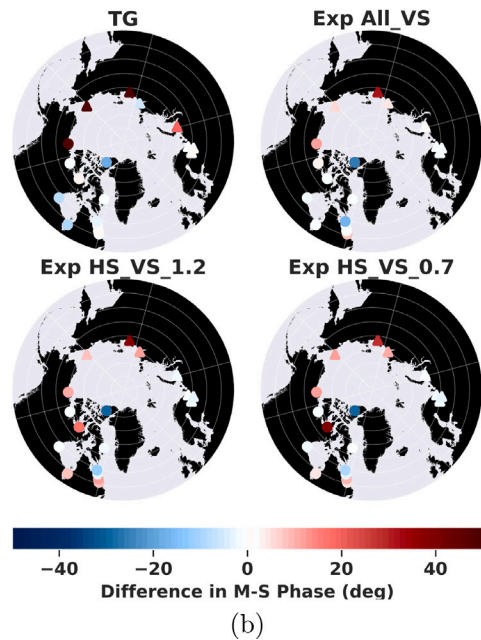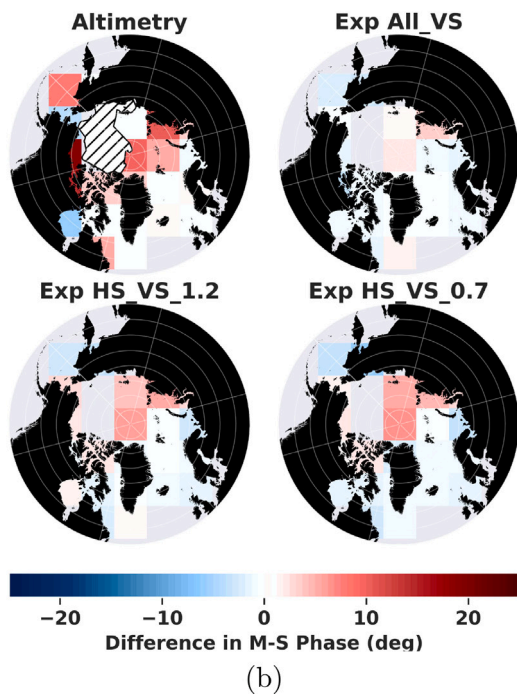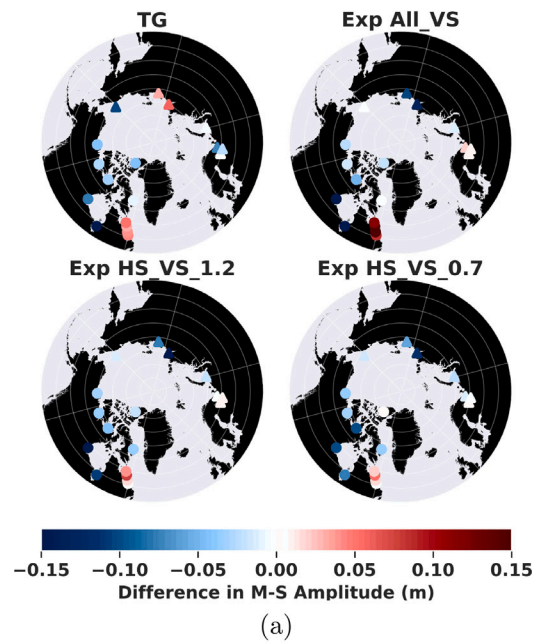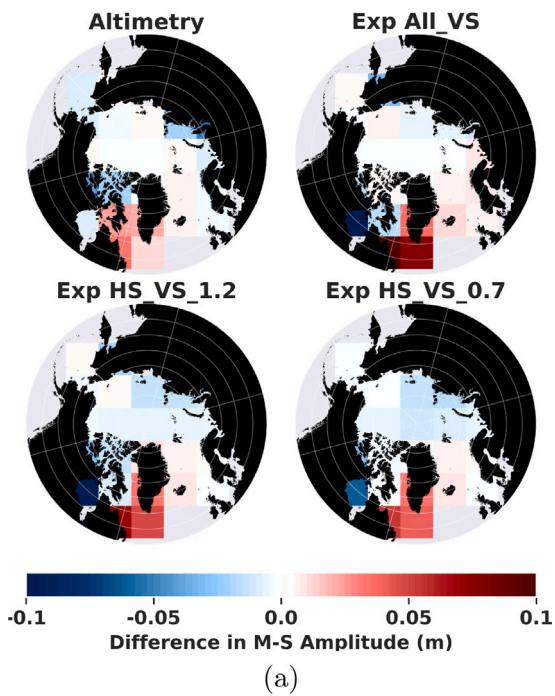
Fig. D.20. March–September differences of M$_2$ tide on a coarse grid for the altimeter-derived product and the Exp All_VS, Exp HS_VS_1.2 and Exp HS_VS_0.7 runs for the year 2019. Differences in amplitude D.20(a) and phase D.20(b). The positive differences (red) denote that the March amplitude is larger/phase is leading than September, while negative differences (blue) denote the opposite.

Fig. D.21. Seasonal Modulation of M$_2$ tide quantified as March–September differences in amplitude and phases for the TG-derived product and the 3 model runs (Exp All_VS, Exp HS_VS_1.2 and Exp HS_VS_0.7) for the year 2012. Differences in amplitude D.21(a) and phase D.21(b). The positive differences (red) denote that the March amplitude is larger/phase is leading than September, while negative differences (blue) denote the opposite.

(a)

(b)
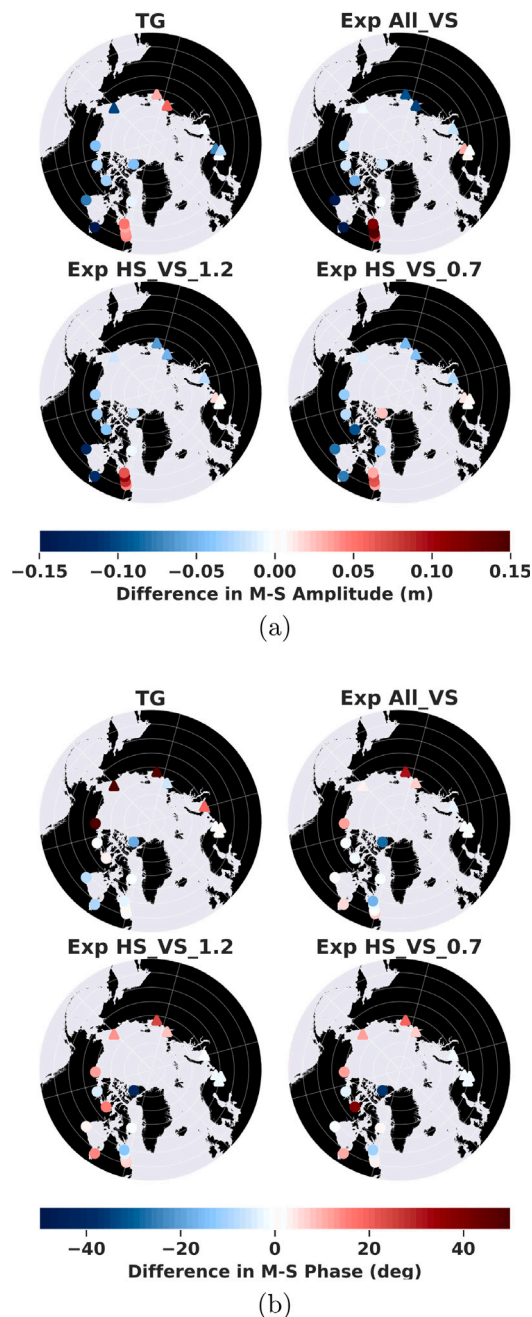
Fig. D.22. Seasonal Modulation of M_2 tide quantified as March–September differences in amplitude and phases for the TG-derived product and the 3 model runs (Exp All_VS, Exp HS_VS_1.2 and Exp HS_VS_0.7) for the year 2017. Differences in amplitude D.22(a) and phase D.22(b). The positive differences (red) denote that the March amplitude is larger/phase is leading than September, while negative differences (blue) denote the opposite.

References

Bij de Vaate, I., Vasulkar, A.N., Slobbe, D.C., Verlaan, M., 2021. The influence of arctic landfast ice on seasonal modulation of the M2 tide. J. Geophys. Res.: Oceans 126 (5), e2020JC016630. http://dx.doi.org/10.1029/2020JC016630.

Brenner, S., Rainville, L., Thomson, J., Cole, S., Lee, C., 2021. Comparing observations and parameterizations of ice-ocean drag through an annual cycle across the beaufort sea. J. Geophys. Res.: Oceans 126 (4), e2020JC016977. http://dx.doi.org/10.1029/2020JC016977, URL: https://onlinelibrary.wiley.com/doi/full/10.1029/2020JC016977.

Cancet, M., Andersen, O.B., Lyard, F., Cotton, D., Benveniste, J., 2018. Arctide2017, a high-resolution regional tidal model in the Arctic Ocean. Adv. Space Res. 62 (6), 1324–1343. http://dx.doi.org/10.1016/J.ASR.2018.01.007.

Chevallier, M., Smith, G.C., Dupont, F., Lemieux, J.F., Forget, G., Fujii, Y., Hernandez, F., Msadek, R., Peterson, K.A., Storto, A., Toyoda, T., Valdivieso, M., Vernieres, G., Zuo, H., Balmaseda, M., Chang, Y.S., Ferry, N., Garric, G., Haines, K., Keeley, S., Kovach, R.M., Kuragano, T., Masina, S., Tang, Y., Tsujino, H., Wang, X., 2017. Intercomparison of the arctic sea ice cover in global ocean–sea ice reanalyses from the ora-ip project. Clim. Dyn. 49 (3), 1107–1136. http://dx.doi.org/10.1007/S00382-016-2985-Y/FIGURES/14, URL: https://link.springer.com/article/10.1007/s00382-016-2985-y.

Codiga, D.L., 2011. Unified Tidal Analysis and Prediction Using the UTide Matlab Functions. Technical Report September, University of Rhode Island, p. 59. http://dx.doi.org/10.13140/RG.2.1.3761.2008.

Collins, A., Hannah, C., Greenberg, D., 2011. Validation of a High Resolution Modelling System for Tides in the Canadian Arctic Archipelago. Can. Tech. Rep., Hydrogr. Ocean Sci., p. 273.

Coon, M., Kwok, R., Levy, G., Pruis, M., Schreyer, H., Sulsky, D., 2007. Arctic ice dynamics joint experiment (AIDJEX) assumptions revisited and found inadequate. J. Geophys. Res.: Oceans 112 (C11), 11–90. http://dx.doi.org/10.1029/2005JC003393.

Copernicus Marine Service, 2019. Global ocean physics reanalysis. In: CMEMS. http://dx.doi.org/10.48670/moi-00021.

Dunphy, M., Dupont, F., Hannah, C., Greenberg, D., 2008. Revisions to a Modelling System for Tides in the Canadian Arctic Archipelago. Can. Tech. Rep., 259, Hydrogr. Ocean Sci, pp. 6–62.

Dupont, F., Hannah, C., Greenberg, D., Cherniawsky, J., Naimie, C., 2002. Modelling system for tides for the Northwest Atlantic Coastal ocean. In: Fisheries & Oceans Canada, Maritimes Region, Ocean Sciences Division, Coastal Ocean Science Section. Technical Report, Bedford Institute of Oceanography.

EUMETSAT Ocean and Facility, Sea Ice Satellite Application, 2022. Global sea ice concentration interim climate data record (v3.0, 2022). http://dx.doi.org/10.15770/EUM_SAF_OSI_0014, OSI-430-a.

Fetterer, F., Knowles, K., Meier, W.N., Savoie, M., Windnagel, A.K., 2017. Sea Ice Index, Version 3 [G02135]. National Snow and Ice Data Center, Boulder, Colorado USA, http://dx.doi.org/10.7265/N5K072F8.

Fisheries and Ocean Canada-MEDS, 2019. Canadian tides and water levels data archive. In: Canadian Hydrographic Service. CHS, URL: https://tides.gc.ca/tides/en/stations.

GEBCO Bathymetric Compilation Group, 2019. The GEBCO_2019 Grid - A Continuous Terrain Model of the Global Oceans and Land. Technical Report, British Oceanographic Data Centre, National Oceanography Centre, NERC, UK.

Heil, P., Hibler, W.D., 2002. Modeling the high-frequency component of Arctic sea ice drift and deformation. J. Phys. Oceanogr. 32 (11), 3039–3057. http://dx.doi.org/10.1175/1520-0485(2002)032<3039:MTHFCO>2.0.CO;2.

Hibler, III, W.D., 1979. A dynamic thermodynamic sea ice model. J. Phys. Oceanogr. 9 (4), 815–846. http://dx.doi.org/10.1175/1520-0485(1979)009<0815:ADTSIM>2.0.CO;2.

Holloway, G., Proshutinsky, A., 2007. Role of tides in arctic ocean/ice climate. J. Geophys. Res.: Oceans 112 (C4), 4–06. http://dx.doi.org/10.1029/2006JC003643.

Hunke, E.C., Dukowicz, J.K., 1997. An elastic–Viscous–plastic model for sea ice dynamics. J. Phys. Oceanogr. 27 (9), 1849–1867. http://dx.doi.org/10.1175/1520-0485(1997)027.

Irazoqui Apecechea, M., Verlaan, M., Zijl, F., Le Coz, C., Kernkamp, H., 2017. Effects of self-attraction and loading at a regional scale: a test case for the northwest European shelf. Ocean Dyn. 67 (6), 729–749. http://dx.doi.org/10.1007/S10236-017-1053-4/TABLES/8, URL: https://link-springer-com.tudelft.idm.oclc.org/article/10.1007/s10236-017-1053-4.

Kagan, B.A., Sofina, E.V., 2010. Ice-induced seasonal variability of tidal constants in the arctic ocean. Cont. Shelf Res. 30 (6), 643–647. http://dx.doi.org/10.1016/J.CSR.2009.05.010.

Kernkamp, H.W., Van Dam, A., Stelling, G.S., De Goede, E.D., 2011. Efficient scheme for the shallow water equations on unstructured grids with application to the Continental Shelf. Ocean Dyn. 61 (8), 1175–1188. http://dx.doi.org/10.1007/S10236-011-0423-6/TABLES/2, URL: https://link-springer-com.tudelft.idm.oclc.org/article/10.1007/s10236-011-0423-6.

Kimmritz, M., Danilov, S., Losch, M., 2016. The adaptive EVP method for solving the sea ice momentum equation. Ocean Model. 101, 59–67. http://dx.doi.org/10.1016/J.OCEMOD.2016.03.004.

Kleptsova, O., Pietrzak, J.D., 2018. High resolution tidal model of Canadian Arctic Archipelago, Baffin and Hudson Bay. Ocean Model. 128, 15–47. http://dx.doi.org/10.1016/j.ocemod.2018.06.001.

Kulikov, M.E., Medvedev, I.P., Kondrin, A.T., 2020. Features of seasonal variability of tidal sea-level oscillations in the Russian Arctic seas. Russ. Meteorol. Hydrol. 45 (6), 411–421. http://dx.doi.org/10.3103/S1068373920060047/FIGURES/3, URL: https://link.springer.com/article/10.3103/S1068373920060047.

Kwok, R., Cunningham, G.F., Hibler, W.D., 2003. Sub-daily sea ice motion and deformation from RADARSAT observations. Geophys. Res. Lett. 30 (23), http://dx.doi.org/10.1029/2003GL018723.

Laikhtman, D., 1958. O vetrovom dreife ledjanykh poley. Trudy Leningradskiy Gidrometeorologicheskiy Institut 7, 129–137.

Landy, J.C., Dawson, G.J., Tsamados, M., Bushuk, M., Stroeve, J.C., Howell, S.E., Krumpen, T., Babb, D.G., Komarov, A.S., Heorton, H.D., Belter, H.J., Aksenov, Y., 2022. A year-round satellite sea-ice thickness record from CryoSat-2. Nature 609 (7927), 517–522. http://dx.doi.org/10.1038/s41586-022-05058-5, URL: https://www.nature.com/articles/s41586-022-05058-5.

Lemieux, J.-F., Tremblay, B., Sedláček, J., Tupper, P., Thomas, S., Huard, D., Auclair, J.P., 2010. Improving the numerical convergence of viscous-plastic sea ice models with the Jacobian-free Newton–Krylov method. J. Comput. Phys. 229 (8), 2840–2852. http://dx.doi.org/10.1016/J.JCP.2009.12.011.

Lepparanta, M., 2011a. Equation of drift ice motion. In: The Drift of Sea Ice. Springer Berlin Heidelberg, pp. 143–185. http://dx.doi.org/10.1007/978-3-642-04683-4{_}6.

Lepparanta, M., 2011b. Free drift. In: The Drift of Sea Ice. Springer Berlin Heidelberg, pp. 185–212. http://dx.doi.org/10.1007/978-3-642-04683-4{_}6.

Lepparanta, M., 2011c. Sea ice rheology. In: The Drift of Sea Ice. Springer Berlin Heidelberg, pp. 107–143. http://dx.doi.org/10.1007/978-3-642-04683-4{_}6.

Lepparanta, M., Omstedt, A., 1990. Dynamic coupling of sea ice and water for an ice field with free boundaries. 42, (4), pp. 482–495. http://dx.doi.org/10.3402/TELLUSA.V42I4.11892, URL: https://www.tandfonline.com/doi/abs/10.3402/tellusa.v42i4.11892.

Li, Z., Zhao, J., Su, J., Li, C., Cheng, B., Hui, F., Yang, Q., Shi, L., 2020. Spatial and temporal variations in the extent and thickness of Arctic landfast ice. Remote Sensing 12 (1), 64. http://dx.doi.org/10.3390/RS12010064.

Lintern, D.G., Macdonald, R.W., Solomon, S.M., Jakes, H., 2013. Beaufort sea storm and resuspension modeling. J. Mar. Syst. 127, 14–25. http://dx.doi.org/10.1016/j.jmarsys.2011.11.015, URL: https://linkinghub.elsevier.com/retrieve/pii/S092479631100282X.

Luneva, M.V., Aksenov, Y., Harle, J.D., Holt, J.T., 2015. The effects of tides on the water mass mixing and sea ice in the Arctic ocean. J. Geophys. Res.: Oceans 120 (10), 6669–6699. http://dx.doi.org/10.1002/2014JC010310.

Lyard, F.H., Allain, D.J., Cancet, M., Carrère, L., Picot, N., 2021. FES2014 global ocean tide atlas: Design and performance. Ocean Sci. 17 (3), 615–649. http://dx.doi.org/10.5194/OS-17-615-2021.

Mahoney, A.R., 2018. Landfast sea ice in a changing Arctic. In: Arctic Report Card 2018. Arctic Program NOAA, pp. 99–109, URL: https://arctic.noaa.gov/Report-Card/Report-Card-2018/ArtMID/7878/ArticleID/788/Landfast-Sea-Ice-in-a-Changing-Arctic.

Mallett, R.D., Stroeve, J.C., Tsamados, M., Landy, J.C., Willatt, R., Nandan, V., Liston, G.E., 2021. Faster decline and higher variability in the sea ice thickness of the marginal Arctic seas when accounting for dynamic snow cover. Cryosphere 15 (5), 2429–2450. http://dx.doi.org/10.5194/TC-15-2429-2021.

Massonnet, F., Goosse, H., Fichefet, T., Counillon, F., 2014. Calibration of sea ice dynamic parameters in an ocean-sea ice model using an ensemble Kalman filter. J. Geophys. Res.: Oceans 119 (7), 4168–4184. http://dx.doi.org/10.1002/2013JC009705, URL: https://onlinelibrary.wiley.com/doi/full/10.1002/2013JC009705.

McPhee, M.G., 1978. A simulation of inertial oscillation in drifting pack ice. Dyn. Atmos. Oceans 2 (2), 107–122. http://dx.doi.org/10.1016/0377-0265(78)90005-2.

McPhee, M.G., 1980. An analysis of pack ice drift in summer. In: Sea Ice Processes and Models. University of Washington Press, pp. 62–75.

McPhee, M., 2017. The sea ice–ocean boundary layer. In: Thomas, D. (Ed.), Sea Ice, third ed. Wiley, pp. 138–159.

Meier, W.N., 2016. Losing arctic sea ice: observations of the recent decline and the long-term context. In: Sea Ice, third ed. John Wiley & Sons, Ltd, pp. 290–303. http://dx.doi.org/10.1002/9781118778371.CH11, URL: https://onlinelibrary.wiley.com/doi/10.1002/9781118778371.ch11.

Muis, S., Verlaan, M., Winsemius, H.C., Aerts, J.C., Ward, P.J., 2016. A global reanalysis of storm surges and extreme sea levels. Nature Commun. 7 (1), 1–12. http://dx.doi.org/10.1038/ncomms11969, URL: https://www.nature.com/articles/ncomms11969.

Müller, M., Cherniawsky, J.Y., Foreman, M.G., Von Storch, J.S., 2014. Seasonal variation of the M 2 tide. Ocean Dyn. 64 (2), 159–177. http://dx.doi.org/10.1007/s10236-013-0679-0, URL: https://link.springer.com/article/10.1007/s10236-013-0679-0.

Ólason, E., Boutin, G., Korosov, A., Rampal, P., Williams, T., Kimmritz, M., Dansereau, V., Samaké, A., 2022. A new brittle rheology and numerical framework for large-scale sea-ice models. J. Adv. Modelling Earth Syst. 14 (8), e2021MS002685. http://dx.doi.org/10.1029/2021MS002685, URL: https://onlinelibrary.wiley.com/doi/full/10.1029/2021MS002685.

Overeem, I., Anderson, R.S., Wobus, C.W., Clow, G.D., Urban, F.E., Matell, N., 2011. Sea ice loss enhances wave action at the Arctic coast. Geophys. Res. Lett. 38, 17503. http://dx.doi.org/10.1029/2011GL048681, URL: http://nsidc.org/data/.

Padman, L., Erofeeva, S., 2004. A barotropic inverse tidal model for the Arctic ocean. Geophys. Res. Lett. 31 (2), http://dx.doi.org/10.1029/2003GL019003.

Pal, N., Barton, K.N., Petersen, M.R., Brus, S.R., Engwirda, D., Arbic, B.K., Roberts, A.F., Westerink, J.J., Wirasaet, D., 2023. Barotropic tides in MPAS-ocean (E3SM V2): impact of ice shelf cavities. Geosci. Model Dev. 16 (4), 1297–1314. http://dx.doi.org/10.5194/GMD-16-1297-2023.

Pease, C.H., Salo, S.A., Overland, J.E., 1983. Drag measurements for first-year sea ice over a shallow sea. J. Geophys. Res.: Oceans 88 (C5), 2853–2862. http://dx.doi.org/10.1029/JC088iC05p02853.

Perovich, D.K., Richter-Menge, J.A., 2009. Loss of sea ice in the Arctic*. Annu. Rev. Mar. Sci. 1, 417–441. http://dx.doi.org/10.1146/ANNUREV.MARINE.010908.163805.

Ray, R.D., 2016. On measurements of the tide at Churchill, Hudson Bay. Atmos.-Ocean 54 (2), 108–116. http://dx.doi.org/10.1080/07055900.2016.1139540.

Ray, R.D., 2022. Technical note: On seasonal variability of the M2 tide. Ocean Sci. 18 (4), 1073–1079. http://dx.doi.org/10.5194/OS-18-1073-2022.

Ricker, R., Hendricks, S., Kaleschke, L., Tian-Kunze, X., King, J., Haas, C., 2017. A weekly Arctic sea-ice thickness data record from merged CryoSat-2 and SMOS satellite data. Cryosphere 11, 1607–1623. http://dx.doi.org/10.5194/tc-11-1607-2017.

Schroeter, S., Sandery, P.A., 2022. Large-ensemble analysis of Antarctic sea ice model sensitivity to parameter uncertainty. Ocean Model. 177, 102090. http://dx.doi.org/10.1016/J.OCEMOD.2022.102090.

Song, P., Sidorenko, D., Scholz, P., Thomas, M., Lohmann, G., 2023. The tidal effects in the finite-volume sea ice-ocean model (FESOM2.1): a comparison between parameterised tidal mixing and explicit tidal forcing. Geosci. Model Dev. 16 (1), 383–405. http://dx.doi.org/10.5194/GMD-16-383-2023.

St-Laurent, P., Saucier, F.J., Dumais, J.F., 2008. On the modification of tides in a seasonally ice-covered sea. J. Geophys. Res.: Oceans 113 (C11), 11014. http://dx.doi.org/10.1029/2007JC004614.

Stammer, D., Ray, R.D., Andersen, O.B., Arbic, B.K., Bosch, W., Carrère, L., Cheng, Y., Chinn, D.S., Dushaw, B.D., Egbert, G.D., Erofeeva, S.Y., Fok, H.S., Green, J.A.M., Griffiths, S., King, M.A., Lapin, V., Lemoine, F.G., Luthcke, S.B., Lyard, F., Morison, J., Müller, M., Padman, L., Richman, J.G., Shriver, J.F., Shum, C.K., Taguchi, E., Yi, Y., 2014. Accuracy assessment of global barotropic ocean tide models. Rev. Geophys. 52 (3), 243–282. http://dx.doi.org/10.1002/2014RG000450, URL: http://doi.wiley.com/10.1002/2014RG000450.

Uotila, P., Goosse, H., Haines, K., Chevallier, M., Barthélemy, A., Bricaud, C., Carton, J., Fučkar, N., Garric, G., Iovino, D., Kauker, F., Korhonen, M., Lien, V.S., Marnela, M., Massonnet, F., Mignac, D., Peterson, K.A., Sadikni, R., Shi, L., Tietsche, S., Toyoda, T., Xie, J., Zhang, Z., 2019. An assessment of ten ocean reanalyses in the polar regions. Clim. Dyn. 52 (3–4), 1613–1650. http://dx.doi.org/10.1007/S00382-018-4242-Z/FIGURES/26, URL: https://link.springer.com/article/10.1007/s00382-018-4242-z.

US National Ice Center, 2020. U.S. national ice center Arctic and Antarctic sea ice concentration and climatologies in gridded format, version 1 [g10033]. In: NSIDC: National Snow and Ice Data Center. http://dx.doi.org/10.7265/46cc-3952, URL: https://nsidc.org/data/g10033/versions/1.

Vasulkar, A., Verlaan, M., Slobbe, C., Kaleschke, L., 2022. Tidal dissipation from free drift sea ice in the barents sea assessed using GNSS beacon observations. Ocean Dyn. 1, 1–21. http://dx.doi.org/10.1007/S10236-022-01516-W.

Verlaan, M., De Kleermaeker, S., Buckman, L., 2015. GLOSSIS: Global storm surge forecasting and information system. In: Australasian Coasts & Ports Conference 2015: 22nd Australasian Coastal and Ocean Engineering Conference and the 15th Australasian Port and Harbour Conference. Engineers Australia and IPENZ, Auckland, New Zealand, pp. 229–234.

Wang, P., Bernier, N.B., 2023. Adding sea ice effects to a global operational model (NEMO v3.6) for forecasting total water level: approach and impact. Geosci. Model Dev. 16 (11), 3335–3354. http://dx.doi.org/10.5194/gmd-16-3335-2023, URL: https://gmd.copernicus.org/articles/16/3335/2023/.

Wang, X., Verlaan, M., Apecechea, M.I., Lin, H.X., 2021. Computation-efficient parameter estimation for a high-resolution global tide and surge model. J. Geophys. Res.: Oceans 126 (3), e2020JC016917. http://dx.doi.org/10.1029/2020JC016917.